









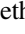
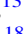
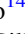



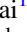





# CMZoom. IV. Incipient High-mass Star Formation throughout the Central Molecular Zone

H Perry Hatchfield<sup>1,2</sup> , Cara Battersby<sup>2,3</sup> , Ashley T. Barnes<sup>4</sup> , Natalie Butterfield<sup>5</sup> , Adam Ginsburg<sup>6</sup> ,  
Jonathan D. Henshaw<sup>7,8</sup> , Steven N. Longmore<sup>7,9,21</sup> , Xing Lu<sup>10</sup> , Brian Svoboda<sup>11</sup> , Daniel Walker<sup>2,12</sup> ,  
Daniel Callanan<sup>3,7</sup> , Elisabeth A. C. Mills<sup>13</sup> , Luis C. Ho<sup>14,15</sup> , Jens Kauffmann<sup>16</sup> , J. M. Diederik Kruijssen<sup>9,17,21</sup> ,  
Jürgen Ott<sup>18</sup> , Thushara Pillai<sup>19</sup> , and Qizhou Zhang<sup>20</sup> 

<sup>1</sup> Jet Propulsion Laboratory, California Institute of Technology, 4800 Oak Grove Drive, Pasadena, CA, 91109, USA

<sup>2</sup> University of Connecticut, Department of Physics, 196A Auditorium Road, Unit 3046, Storrs, CT 06269 USA

<sup>3</sup> Center for Astrophysics | Harvard & Smithsonian, MS-78, 60 Garden Street, Cambridge, MA 02138 USA

<sup>4</sup> Argelander-Institut für Astronomie, Universität Bonn, Auf dem Hügel 71, D-53121, Bonn, DE, Germany

<sup>5</sup> National Radio Astronomy Observatory, 520 Edgemont Road, Charlottesville, VA 22903, USA

<sup>6</sup> University of Florida Department of Astronomy, Bryant Space Science Center, Gainesville, FL, 32611, USA

<sup>7</sup> Astrophysics Research Institute, Liverpool John Moores University, 146 Brownlow Hill, Liverpool L3 5RF, UK

<sup>8</sup> Max-Planck-Institute for Astronomy, Königstuhl 17, D-69117 Heidelberg, Germany

<sup>9</sup> Cosmic Origins Of Life (COOL) Research DAO, Munich, Germany

<sup>10</sup> Shanghai Astronomical Observatory, Chinese Academy of Sciences, 80 Nandan Road, Shanghai 200030, People's Republic of China

<sup>11</sup> National Radio Astronomy Observatory, P.O. Box O, Socorro, NM 87801 USA

<sup>12</sup> UK ALMA Regional Centre Node, Jodrell Bank Centre for Astrophysics, The University of Manchester, Manchester M13 9PL, UK

<sup>13</sup> Department of Physics and Astronomy, University of Kansas, 1251 Wescoe Hall Drive, Lawrence, KS 66045, USA

<sup>14</sup> Kavli Institute for Astronomy and Astrophysics, Peking University, Beijing 100871, People's Republic of China

<sup>15</sup> Department of Astronomy, School of Physics, Peking University, Beijing 100871, People's Republic of China

<sup>16</sup> Haystack Observatory, Massachusetts Institute of Technology, 99 Millstone Road, Westford, MA 01886, USA

<sup>17</sup> Technical University of Munich, School of Engineering and Design, Department of Aerospace and Geodesy, Chair of Remote Sensing Technology, Arcisstr. 21, D-80333 Munich, Germany

<sup>18</sup> National Radio Astronomy Observatory, 1003 Lopezville Road, Socorro, NM 87801, USA

<sup>19</sup> Boston University Astronomy Department, 725 Commonwealth Avenue, Boston, MA 02215, USA

<sup>20</sup> Center for Astrophysics | Harvard & Smithsonian, MS-42, 60 Garden Street, Cambridge, MA 02138 USA

Received 2023 March 17; revised 2023 October 24; accepted 2023 November 1; published 2024 February 1

## Abstract

In this work, we constrain the star-forming properties of all possible sites of incipient high-mass star formation in the Milky Way's Galactic Center. We identify dense structures using the CMZoom 1.3 mm dust continuum catalog of objects with typical radii of  $\sim 0.1$  pc, and measure their association with tracers of high-mass star formation. We incorporate compact emission at 8, 21, 24, 25, and 70  $\mu\text{m}$  from the Midcourse Space Experiment, Spitzer, Herschel, and SOFIA, cataloged young stellar objects, and water and methanol masers to characterize each source. We find an incipient star formation rate (SFR) for the Central Molecular Zone (CMZ) of  $\sim 0.08 M_{\odot} \text{ yr}^{-1}$  over the next few  $10^5$  yr. We calculate upper and lower limits on the CMZ's incipient SFR of  $\sim 0.45$  and  $\sim 0.05 M_{\odot} \text{ yr}^{-1}$ , respectively, spanning roughly equal to and several times greater than other estimates of CMZ's recent SFR. Despite substantial uncertainties, our results suggest the incipient SFR in the CMZ may be higher than previously estimated. We find that the prevalence of star formation tracers does not correlate with source volume density, but instead  $\gtrsim 75\%$  of high-mass star formation is found in regions above a column density ratio ( $N_{\text{SMA}}/N_{\text{Herschel}}$ ) of  $\sim 1.5$ . Finally, we highlight the detection of *atoll sources*, a reoccurring morphology of cold dust encircling evolved infrared sources, possibly representing H II regions in the process of destroying their envelopes.

*Unified Astronomy Thesaurus concepts:* Star formation (1569); Galactic center (565); Milky Way Galaxy (1054); Young stellar objects (1834); Protostars (1302)

*Supporting material:* figure set, machine-readable tables

## 1. Introduction

Understanding how the process of star formation varies with environment demands a detailed study of molecular cloud evolution under diverse physical conditions. Star-forming regions in the solar neighborhood provide an extremely detailed look at the formation of stars in one relatively narrow window of physical

parameter space. The interstellar medium (ISM) occupying the radially innermost few hundred parsecs of the Milky Way provides an excellent opportunity to observe the formation of stars within molecular clouds subject to a more extreme environment than that of the galaxy's disk, while still being nearby enough for modern observatories to resolve the fine details of the star formation process. The substantial reservoir of gas surrounding the Galactic Center at a radius of about 100 pc known as the Central Molecular Zone (CMZ) hosts more than  $3 \times 10^7 M_{\odot}$  of molecular hydrogen (e.g., Dahmen et al. 1998; Ferrière et al. 2007), largely contained in giant molecular clouds with volume densities commonly exceeding  $10^4 \text{ cm}^{-3}$  (e.g., Guesten & Downes 1982; Mills et al. 2018), high (50–100 K) kinetic temperatures (e.g., Ginsburg et al. 2016;

<sup>21</sup> coolresearch.io.

Krieger et al. 2017), broad turbulent velocity dispersions ( $\sim 10 \text{ km s}^{-1}$ ), and complex three-dimensional morphologies (e.g., Shetty et al. 2012; Henshaw et al. 2016; Kauffmann et al. 2017a; Henshaw et al. 2019). These conditions bear some resemblance to the properties of  $z \sim 1\text{--}3$  galaxies near the apex of cosmic star formation, and might be used to further our understanding of how star formation occurs in the distant reaches of the universe (e.g., Kruijssen & Longmore 2013).

Over the last decade, studies measuring the star formation rate (SFR) within the Galactic Center have revealed a global dearth of recent star formation relative to the substantial dense gas content (e.g., Immer et al. 2012; Longmore et al. 2013a; Barnes et al. 2017; Lu et al. 2019a). There are, however, plentiful signposts of vigorous past and ongoing high- and low-mass star formation throughout the CMZ (e.g., Ginsburg et al. 2018; Walker et al. 2018; Lu et al. 2020, 2021; Walker et al. 2021). The composition of the nuclear stellar disk implies periods of much higher SFR within the past  $\sim 1$  Gyr (Nogueras-Lara et al. 2020), and the presence of the Arches and Quintuplet star clusters, thought to have been formed within the last  $\sim 6$  Myr (e.g., Figer et al. 2002; Hosek et al. 2019), suggests that the CMZ has a prolific and irregular star formation history. Some theoretical studies bolster these claims, showing that computational models of the Milky Way’s CMZ display highly episodic star formation histories on similar timescales (e.g., Kruijssen et al. 2014; Krumholz & Kruijssen 2015; Krumholz et al. 2017; Torrey et al. 2017; Armillotta et al. 2019; Orr et al. 2021).

There are several clouds containing young massive clusters (with total masses  $\gtrsim 10^4 M_\odot$ ) actively forming throughout the CMZ, most notably in Sgr B2, Dust Ridge Clouds C and E, and Sgr C (e.g., Schmiedeke et al. 2016; Walker et al. 2016; Ginsburg et al. 2018; Walker et al. 2018; Lu et al. 2019a, 2019b; Barnes et al. 2019; Lu et al. 2021). However, these clouds are only a subset of a population of massive molecular clouds with extremely high densities, many of which appear to have few if any signatures of high-mass star formation (e.g., Longmore et al. 2013a; Lu et al. 2019a; Walker et al. 2021; Williams et al. 2022). In order to understand the global deficiency of active star formation in the CMZ relative to its total dense gas mass, we must consider the complete sample of giant molecular clouds throughout the CMZ.

CMZoom (Battersby et al. 2020) is the first survey to map all high-density ( $N(\text{H}_2) > 10^{23} \text{ cm}^{-2}$ ) gas at 1.3 mm in the CMZ with sufficient resolution and sensitivity to uncover their dense gas substructure on sub-parsec scales. The survey’s catalog of compact sources, constructed from the Submillimeter Array (SMA)’s 1.3 mm dust continuum emission, characterized all possible sites of ongoing and incipient high-mass star formation, placing an upper limit on the present-day star formation potential of the Galactic Center (Hatchfield et al. 2020). However, from CMZoom’s 1.3 mm dust continuum alone, it is impossible to determine which of these compact submillimeter sources are actively forming high-mass protostars and which remain quiescent.

In this paper, we perform a detailed analysis of each CMZoom source, incorporating previous multiwavelength observations and catalogs of star formation tracers from the literature to characterize the properties of each possible site of deeply embedded, incipient high-mass star formation in the Galactic Center (excluding Sgr A\* and Sgr B2). In Section 2, we briefly summarize the details of the CMZoom survey and

describe the design of the CMZoom catalog. In Section 3, we describe our method for comparing CMZoom objects with compact far-IR sources and previous catalogs of young stellar object (YSO) candidates and masers. In Section 4, we present our results for which CMZoom clouds host ongoing massive star formation, and how the physical properties of the sources correlate with the indicators of active star formation. In Section 5, we discuss the implications of these results, focusing on the scaling relationships and SFRs presented in the previous section. Finally, in Section 6, we summarize the results of this work and list our key conclusions.

## 2. Summary of the Data and Catalog Design

The CMZoom survey is an SMA large program, surveying all dense gas ( $N(\text{H}_2) > 10^{23} \text{ cm}^{-2}$ ) in the CMZ. Using the compact and subcompact configurations of the SMA, the 1.3 mm continuum emission achieved a typical resolution of  $\sim 3''$  ( $\sim 0.1 \text{ pc}$ ), revealing a wealth of differing morphologies and complexities of dust structure in the 35 regions and  $\sim 240 \text{ arcmin}^2$  ( $\sim 1360 \text{ pc}^2$ ) area surveyed. In addition to the continuum, CMZoom surveyed emission from notable transitions of key molecular species, such as CO(2–1) and its isotopologue companions, the para- $\text{H}_2\text{CO}$  triplet transitions ( $2_{0,3} - 1_{0,2}$ ,  $2_{2,2} - 1_{2,1}$ ,  $2_{2,1} - 1_{2,0}$ ), SiO(5–4) and others, presented in Callanan et al. (2023). While the vast majority of regions observed by CMZoom have been confirmed to be near the Galactic Center using a variety of methods, including their spectral properties, a handful of regions (4 of 36) cannot be definitively localized to the CMZ and may represent foreground emission. These sources (G0.393, G0.212, G1.670, and G359.137) have been flagged as possible foreground regions, though they have been included in the following analysis for completeness.

The dust continuum catalog, detailed in Hatchfield et al. (2020), was designed to characterize the properties of the compact dust emission structures throughout the CMZ’s dense gas content as completely as possible using a pruned dendrogram. We produce a hierarchical decomposition of the flux represented by a dendrogram (implemented using `astro-dendro`<sup>22</sup>), a tree-like plot where the highest level, brightest structures are identified as *leaves*. The significance of each of these leaves is determined by a global estimate of the noise,  $\sigma_{\text{global}}$ , with a minimum structure boundary value of  $3\sigma$  and a minimum leaf boundary significance of  $1\sigma_{\text{global}}$ . The dendrogram algorithm also considers a minimum pixel size for leaves, which we have chosen to be half the typical beam size. There is no enforced maximum leaf size, and the shapes and sizes of the resulting leaves are entirely determined by the significance and extent of local maxima in the flux map and the dendrogram parameters described above. The dynamic range and variable noise across the surveyed regions necessitated the *pruning* of this initial dendrogram, in which leaves were removed from the final catalog if they did not meet a local noise threshold in the mean flux and peak flux. Local rms noise estimates were constructed from the SMA residual maps. The only leaves that remain in the catalog are those that have a peak flux of  $6\sigma$  above the local rms noise, and a mean flux of  $2\sigma$  above the local rms. The resulting catalog is uniquely reproducible from the input dust continuum mosaic and residuals. The interpretation of these leaves is complicated by their physical scale and

<sup>22</sup> <http://www.dendrograms.org/>

**Table 1**  
Brief Summary of Which Data Are Used as Tracers of Incipient and Ongoing Star Formation in This Work

Star Formation Tracer	Astrometric Uncertainty	Citation
8 $\mu\text{m}$ pointlike emission	...	Benjamin et al. (2003)
21 $\mu\text{m}$ pointlike emission	...	Egan et al. (2003)
24 $\mu\text{m}$ pointlike emission	...	Carey et al. (2009)
70 $\mu\text{m}$ pointlike emission	...	Molinari et al. (2010, 2011)
Prev. cataloged 70 $\mu\text{m}$ point sources	5''	Molinari et al. (2016)
Prev. cataloged 24 $\mu\text{m}$ point sources	6''	Gutermuth & Heyer (2015)
H <sub>2</sub> O Masers ( $J = 6_{1,6} - 5_{2,3}$ )	1''	Walsh et al. (2014)
CH <sub>3</sub> OH Masers (6.7 GHz)	0''6	Caswell et al. (2010)
Prev. cataloged YSOs	2''–6''	An et al. (2011); Immer et al. (2012)

the SMA’s physical resolution at the Galactic Center, as the emission from these leaves is likely due to a combination of unresolved protostellar sources and resolved dusty envelopes. Atacama Large Millimeter/submillimeter Array (ALMA) observations of a subset of the CMZoom leaves have revealed a population of multiple protostellar sources that are unresolved by the SMA, so in this work, we interpret the star-forming sources in the catalog as protoclusters containing one or more high-mass protostars (e.g., Ginsburg et al. 2018; Barnes et al. 2019; Walker et al. 2021).

The flux and mass completeness of this catalog were determined using synthetic interferometric observations of clouds of point-source-like dust sources, and replicating the imaging pipeline used to process the observed dust continuum maps of the CMZoom data products. Hatchfield et al. (2020) use these synthetic observations to estimate that more than 95% of dust continuum sources with masses above  $80 M_{\odot}$  have been recovered by this cataloging procedure and are characterized in the high-robustness version of the CMZoom catalog (assuming an average dust temperature of at least 20 K across the entire dendrogram leaf). Using this mass completeness, given an initial mass function (IMF, e.g., Kroupa 2001) and an assumed star formation efficiency (SFE) for star-forming structures on scales resolved by the SMA, this mass completeness limit suggests that virtually all (more than 95%) of possible sites of deeply embedded high-mass star formation within the CMZ are included within the CMZoom catalog. While the CMZoom survey does not observe the entire contiguous spatial range of the CMZ, it does sample all regions above a Herschel-inferred column density of  $10^{23} \text{ N(H}_2\text{) cm}^2$ , and therefore, is almost certain to capture the deeply embedded high-mass star formation present in this extreme part of the Galaxy (Battersby et al. 2020). It must also be noted that the catalog does not include star-forming sources that are sufficiently evolved to destroy their cold and dusty molecular envelopes, though such sources account for a large portion of the star formation tracers throughout the CMZ considered in the other work cited throughout. The present analysis aims to characterize an earlier stage of star formation, during which the young protoclusters are still embedded in their cold envelopes.

### 3. Method

#### 3.1. Selection and Identification of Star Formation Tracers

By comparing the positions and properties of the CMZoom catalog leaves with the positions of a variety of previously cataloged tracers of active or recent star formation, we determine the incipient SFR for each source in the CMZoom survey. The presence of certain maser species is known to trace

recent star formation within molecular clouds. In particular, emission at 6.7 GHz from methanol (CH<sub>3</sub>OH) masers indicates ongoing high-mass ( $M > 8 M_{\odot}$ ) star formation (e.g., Minier et al. 2003; Xu et al. 2008). Water (H<sub>2</sub>O) masers are commonly associated with both high- and low-mass star-forming regions, but may also indicate the presence of evolved sources on the asymptotic branch of asymptotic giant branch stars, Mira variables, and possibly other astrophysical phenomena (e.g., Hinkle & Barnes 1979; Forster & Caswell 1999; Miranda et al. 2001), but such sources will be much dimmer and can be excluded based on their emission in other wave bands (Longmore et al. 2013b). We consider the coincidence of methanol or H<sub>2</sub>O masers with CMZoom catalog objects as an indication that those leaves are actively forming high-mass stars. We incorporate the 6.67 GHz emission from CH<sub>3</sub>OH masers cataloged using the Parkes telescope by Caswell et al. (2010) and the  $J = 6_{1,6} - 5_{2,3}$  transition of H<sub>2</sub>O masers cataloged using the Australia Telescope Compact Array by Walsh et al. (2014). If a CMZoom catalog leaf’s contour overlaps with one of the masers from either of these catalogs within the reported astrometric uncertainty (see Table 1), it is considered associated and the leaf is considered to have a robust signature of active star formation. While deeper- and higher-resolution maser observations are available for a subset of the CMZoom area (e.g., Lu et al. 2015, 2019a), we do not include the analysis of these data here in order to preserve a consistent approach across all regions in the survey.

We must consider that these masers may not be present or detectable at all sites and evolutionary stages of incipient star formation, so we also consider the presence of mid- and far-IR continuum emission from the dusty envelopes of young protoclusters. The presence of pointlike far-IR emission between 20 and 70  $\mu\text{m}$  associated with a compact submillimeter dust source is a signature of early high-mass star formation (e.g., Yusef-Zadeh et al. 2008), since the spectral energy distributions (SEDs) of dust surrounding Class 0 and I protostars peak in the far-IR. While some populations of evolved stars may display similar far-IR profiles, potentially masquerading as high-mass YSOs, these compact far-IR sources that are associated with cold, dense submillimeter gas structures are much less likely to be interlopers (e.g., Schultheis et al. 2003; An et al. 2011; Koepferl et al. 2015).

Past surveys have cataloged pointlike infrared sources according to a variety of other criteria, identifying a large number of YSO candidates throughout the Galactic Center. Here, we cross-correlate the locations of 24 and 70  $\mu\text{m}$  pointlike sources identified by Gutermuth & Heyer (2015) and Molinari et al. (2016), respectively. The 24  $\mu\text{m}$  point-source catalog presented by Gutermuth & Heyer (2015) using

data from the MIPS GAL Survey (Carey et al. 2009) is constructed using `PhotVis`, a modification of the `DAOFIND` algorithm (Stetson 1987; Gutermuth et al. 2008). CMZoom sources with a leaf contour overlapping within one MIPS GAL beam (as used in generating the catalog,  $6''.25$  FWHM) are considered associated with the YSO candidate and thus are considered robustly star forming. The  $70\ \mu\text{m}$  point-source catalog generated from the Hi-Gal survey (Molinari et al. 2010, 2016) is generated using the `CuTex` algorithm, which fits 2D Gaussians to perform photometry by considering the curvature of the flux map (Molinari et al. 2011). Any CMZoom sources whose leaf contour overlaps within one Hi-Gal beam FWHM ( $\sim 5''$ ) of these sources are considered associated.

We perform the same general procedure for several previous catalogs of YSO candidates throughout the survey region. An et al. (2011) identify YSO candidates from the infrared point-source catalog presented in Ramírez et al. (2008) using spectra from  $5\text{--}35\ \mu\text{m}$  from the Infrared Spectrograph (IRS) of the Spitzer space telescope. Yusef-Zadeh et al. (2009) use  $24$  and  $70\ \mu\text{m}$  observations with Spitzer/MIPS, supplemented by other far-IR, submillimeter, and radio observations to identify a large sample of YSOs in the Galactic Center, though this sample is likely contaminated with a significant fraction of evolved stars interacting with surrounding dust (Koeperl et al. 2015). Lastly, we consider the YSO catalog produced by Immer et al. (2012) by analyzing SEDS observed with IRS toward point sources identified using ISOGAL (Omont et al. 2003; Schuller et al. 2003). For each of these previous YSO catalogs, we determine their association with the CMZoom sources using the beam FWHM from the corresponding instruments as the corresponding astrometric uncertainty. Leaves with contours overlapping within the positional uncertainty of these YSOs are flagged as robustly star forming.

### 3.2. Cataloging of Compact Far-IR Sources by Eye

To supplement the previously noted sources in the far-IR, we performed a by-eye search for pointlike emission in the  $8$ ,  $21$ ,  $24$ , and  $70\ \mu\text{m}$  dust continuum mosaics (shown in Figures 1 and 2) associated with each CMZoom robust catalog source. This combination of determining association with star formation tracers algorithmically as well as by eye is helpful because the far-IR dust continuum landscape of the Galactic Center is very complex, with highly variable background levels and noise properties, significant potential for confusion with foreground sources, and bright extended emission that is not necessarily associated with sites of early star formation. Performing a by-eye survey allows us to handle ambiguous cases that may have been missed or mischaracterized in previous studies on an individual basis, while using independent selection criteria.

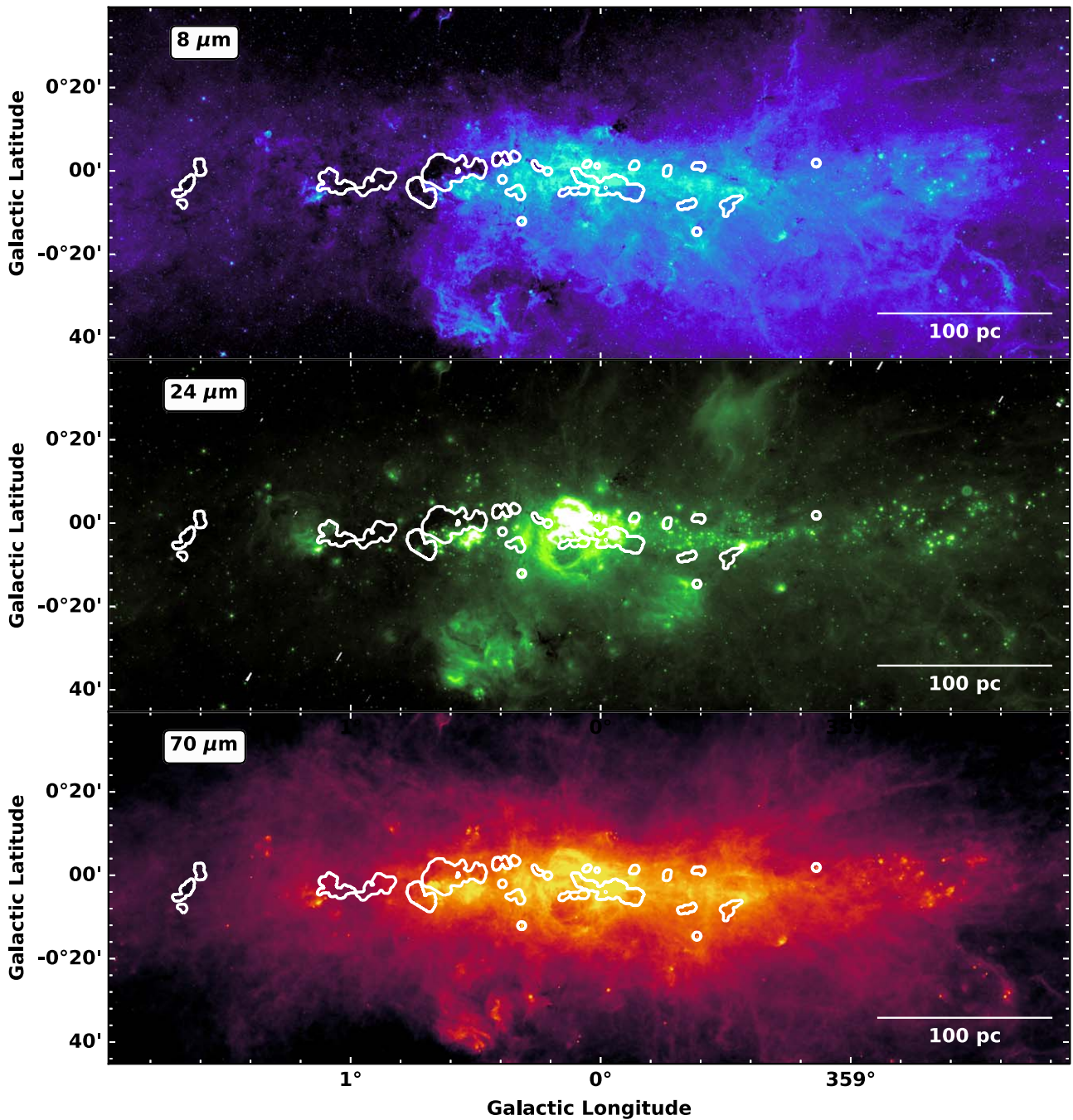
The goal of this search was to robustly identify the presence or absence of any signature of active high-mass star formation. To further mitigate the inherent biases of human error in performing this by-eye cataloging, eight team members (initials H.H., C.B., A.B., N.B., S.L., X.L., B.S., and D.W.) performed the task independently. Each team member, using locally scaled red, green, and blue maps (R:  $70\ \mu\text{m}$ , G:  $21$  and  $24\ \mu\text{m}$  and B:  $8\ \mu\text{m}$ , e.g., Figure 2), designated either a *robust detection*, *robust non-detection*, or *ambiguous detection* for each star formation tracer, for each of the 285 high-robustness catalog sources. A final determination of robustly star-forming, *robustly non-star forming* (or, equivalently, *robustly quiescent*), and *ambiguous*

*star-forming state* was then decided considering the compilation of the independent results. Leaves with significant consensus (at least six of the seven team members in agreement) for a certain designation for  $70$ ,  $21$ , or  $24\ \mu\text{m}$  pointlike sources were considered to be robustly star forming or robustly quiescent, corresponding to the consensus. Leaves for which significant disagreement was recorded ( $\geq 2$  disagreeing on designations) were reinspected to determine if there was a discernible cause for the discrepancy, or if the leaf should be designated as *ambiguous*. The most prevalent cases for ambiguity are marginally compact sources embedded in or near bright, structured extended emission. While it is possible that these ambiguous sources are actively star forming, their properties cannot be easily distinguished from their envelope emission, and higher-resolution and sensitivity measurements or more sophisticated fitting techniques (e.g., Immer et al. 2012) would be necessary to arrive at a more definitive designation. Therefore, such leaves are designated as ambiguously star forming in the following analysis.

### 3.3. Sources of Uncertainty in the By-eye Analysis

In identifying the association of each high-mass star formation tracer with the catalog leaves, there are several opportunities for ambiguity and uncertainty that must be addressed. While the majority of sources designated as robustly star-forming or robustly quiescent had a near-unanimous agreement about the presence or absence of each star formation tracer, ambiguous edge cases were reinspected by eye by only one team member, compiling the previous results and reaching a final designation based on the relevant context. It is clear that this final designation for the cases handled in this way might be biased, but such edge cases largely fell into two categories. First, for regions with bright but diffuse emission suffusing the leaf contours and their immediate surroundings with non-point-source-like substructure, some team members marked leaves as having compact far-IR emission. Second, some leaf contours overlap with, but are not centered on a bright, far-IR compact source, and some team members marked such leaves as non-star forming. The final designation for leaves in both cases was ambiguously star forming unless other information was available to better constrain their properties.

The by-eye component of the star formation tracer cataloging does not significantly alter the statistics of the final populations. Only 11 CMZoom leaves achieved a robustly star-forming designation without association with a previously cataloged star formation tracer, of which 10 are in immediate proximity, though not overlapping with, a previously cataloged tracer. The remaining source, G0.619+0.012i, hosts a clear  $8\ \mu\text{m}$  point source and a much more subtle  $24\text{--}25\ \mu\text{m}$  point source, visible in both MIPS GAL and SOFIA FORCAST continuum observations. Because of the low signal-to-noise value for this far-IR source, it is possible that previous automatic cataloging algorithms have missed it, and the presence of a cold  $1.3\ \text{mm}$  continuum envelope better highlights its likely protostellar nature. While many of the more ambiguously star-forming sources may correspond to previously not-cataloged YSO candidates, characterizing their nature is left for future efforts using a more complete set of observations.



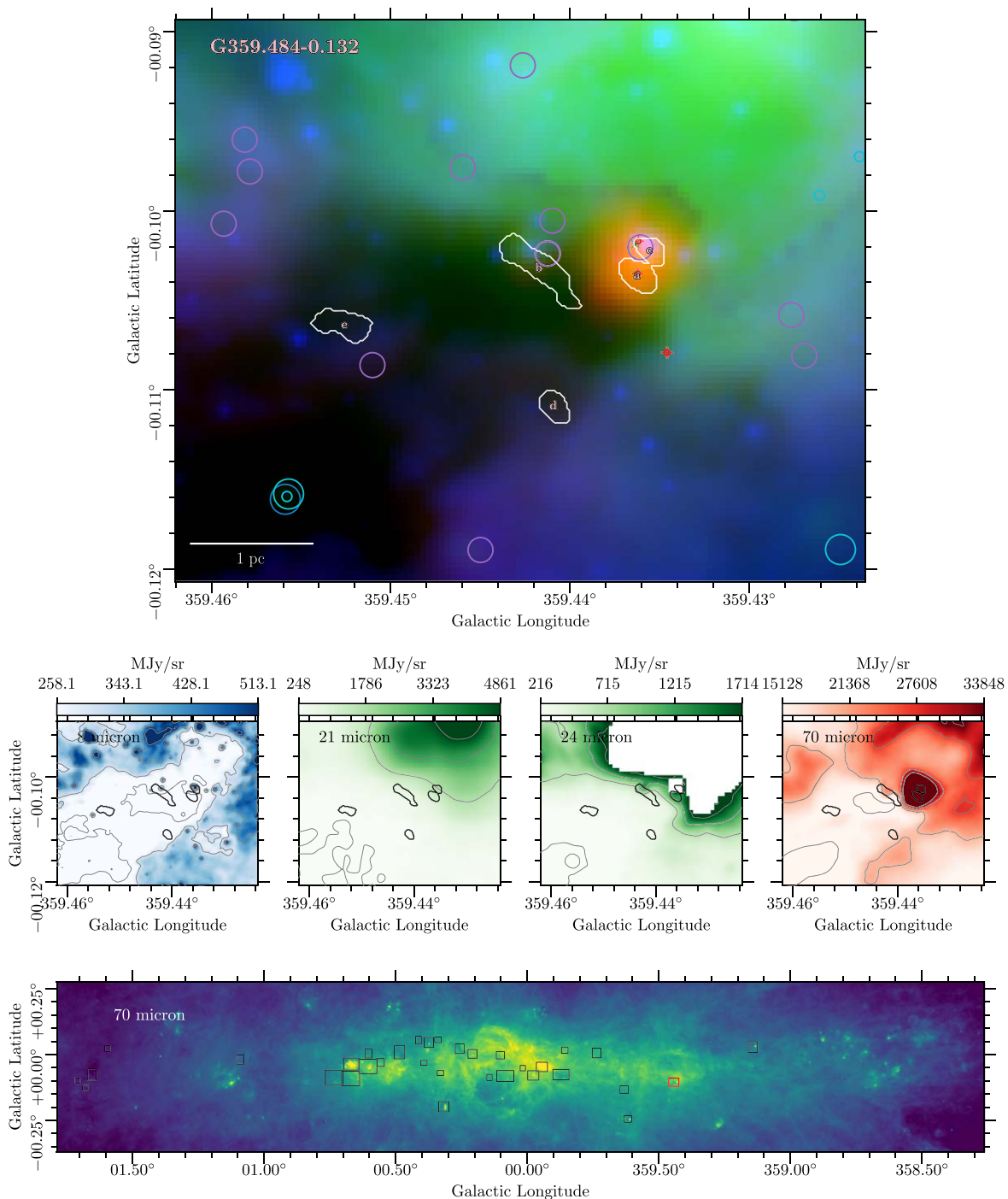
**Figure 1.** Mosaics of the innermost  $4^\circ$  of the CMZ constructed from  $8\ \mu\text{m}$  (B),  $24\ \mu\text{m}$  (G), and  $70\ \mu\text{m}$  (R) continuum from GLIMPSE (top, Benjamin et al. 2003), MIPS GAL (middle, Carey et al. 2009), and Herschel’s Hi-GAL survey (bottom, Molinari et al. 2010), respectively. Contours in white are overlaid showing the CMZoom survey footprint in each panel. Many of the pointlike emission sources in each panel are largely more evolved star-forming sources than the dusty enveloped sources considered in this work or main-sequence stars embedded in the ambient medium of the CMZ (e.g., Koepferl et al. 2015).

### 3.4. Accounting for Saturated Pixels with SOFIA FORCAST Data

Several regions in the CMZoom field are saturated in the  $24\ \mu\text{m}$  emission map from Spitzer/MIPS (see Section 5.2 in Carey et al. 2009). Because these saturated sources in the MIPS GAL field are typically associated with compact, bright far-IR sources, some are particularly relevant to the present study. We consider lower-resolution  $21\ \mu\text{m}$  maps from the Midcourse Space Experiment (MSX; Egan et al. 2003) in cases of saturation in the MIPS GAL maps. In the most complex regions of the CMZ’s warm dust component, the additional

spatial resolution gained by considering more recent observations from other instruments is critical for distinguishing the star-forming properties of the relevant CMZoom catalog objects.

To that end, we use data from the FORCAST Galactic Center Legacy Survey (Hankins et al. 2019, 2020) to characterize the compact  $25.3\ \mu\text{m}$  emission associated with the 34 CMZoom catalog objects for which Spitzer/MIPS data are saturated. An example of such a region is shown in Figure 3. Using these data, we confirm whether the CMZoom sources host signatures of high-mass star formation. Several

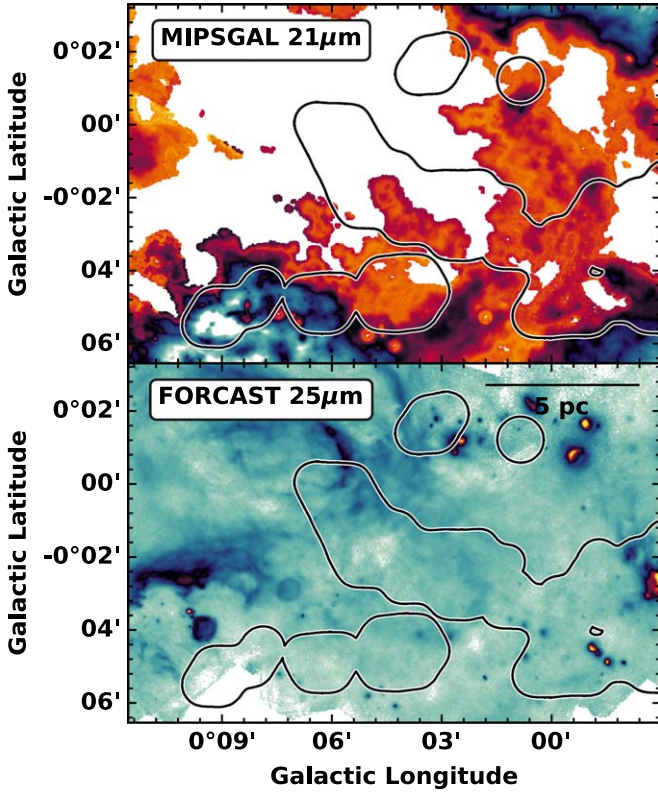


**Figure 2.** An example (Sgr C) of the three-color images used in the by-eye search for compact emission signifying the early onset of star formation associated with CMZoom catalog objects. The three colors used in the top panel are  $8\ \mu\text{m}$  (blue, GLIMPSE, from Benjamin et al. (2003)),  $24\ \mu\text{m}$  (green, MIPS GAL, from Carey et al. 2009), and  $70\ \mu\text{m}$  (red, Hi-Gal, from Molinari et al. 2010)). These are each shown individually in the bottom four panels, along with the  $21\ \mu\text{m}$  emission from MSX (Egan et al. 2003). Overlaid on the composite three-color image are white contours outlining the CMZoom leaves, along with cyan circles demarcating YSO candidates from a compilation of those identified by Yusef-Zadeh et al. (2009), An et al. (2011), and Immer et al. (2012), purple circles indicating the  $70\ \mu\text{m}$  point sources cataloged by Molinari et al. (2010), and darker blue circles representing the point sources identified by Gutermuth & Heyer (2015). The radial size of these circles corresponds to the FWHM condition used to determine plausible association with CMZoom leaves. The bottom panel shows a  $70\ \mu\text{m}$  mosaic of the Galactic Center with each CMZoom region shown as a black box, with the specific region from the above panels highlighted in red. In this case, leaves a, b, and c are labeled as having robust signatures of high-mass star formation, and have been flagged as robustly star-forming in the catalog, while leaves d and e are labeled robustly quiescent. The complete figure set (33 images) is available in the online journal. Note that in the figure set, region numbers do not correspond to the mask numbers referenced in the tables throughout the rest of this work.

(The complete figure set (33 images) is available.)

key CMZoom clouds are not covered by the SOFIA FORCAST Galactic Center Survey (most notably the  $1^\circ.6$  cloud complex, the  $50\ \text{km s}^{-1}$  cloud, and the Dust Ridge

clouds), so this analysis is not available for all leaves in the catalog. This may lead to a potential bias in the identified star-forming sources, as it is possible that higher-resolution



**Figure 3.** A comparison of the MIPS GAL (top panel) and SOFIA FORCAST (bottom panel) observations toward a subset of CMZoom fields near the Galactic nucleus, including “The Three Little Pigs” and “The 50 km s<sup>-1</sup> Cloud.” The saturated regions in MIPS GAL are resolved with FORCAST, though the FORCAST Galactic Center Survey does not cover all regions observed by CMZoom, and so could not be applied to the entire catalog sample.

measurements with greater sensitivity to far-IR point sources from SOFIA’s FORCAST instrument or future observatories would reveal even more compact emission within seemingly quiescent CMZoom catalog leaves. Future analysis will be expanded to include a more detailed characterization of the CMZoom sources using the data available from the FORCAST Galactic Center Legacy Survey.

### 3.5. Summary of the Method Used for Star Formation Designation

For the sake of clarity, here we concisely summarize the procedure for identifying which of the CMZoom sources are robustly star forming, robustly quiescent, and ambiguously star forming. A source is considered robustly star forming if it has:

1. A previously identified YSO within its leaf contour, within the uncertainty of the YSO’s position,
2. A previously cataloged H<sub>2</sub>O or CH<sub>3</sub>OH maser within its leaf contour, up to the maser’s positional uncertainty,
3. A previously cataloged 24 μm or 70 μm point source overlapping the leaf contour, within the beam of the corresponding observation,
4. A by-eye determined pointlike source of 21, 24, 25, or 70 μm emission overlapping with the leaf contour.

A source is designated as robustly quiescent if it has none of the above signatures of high-mass star formation. Finally, a source is considered ambiguously star forming if any of the above criteria are ambiguously valid, or if the by-eye

designation was clouded by bright and diffuse emission surrounding the source.

## 4. Results

### 4.1. Star-forming Properties of CMZoom Sources

The expansion of the CMZoom catalog produced via the methods described in the previous section has been made available online on the CMZoom database, along with the rest of the survey’s data products.<sup>23</sup> With this compiled catalog of deeply embedded star formation throughout the CMZ, we can consider the physical properties of the CMZoom leaves in the context of their star-forming status. The properties we consider here are those reported in the CMZoom survey’s high-robustness catalog,<sup>24</sup> and their calculation is fully explained in Hatchfield et al. (2020), though we briefly review several key definitions here.

The compact dust sources resolved by CMZoom are defined as the leaves of the dendrogram produced by the `astro-dendro` algorithm applied to the entire survey mosaic, and do not necessarily display elliptical boundary contours. We consider the effective radius of each source to be  $R_{\text{eff}} \equiv (N_{\text{pix}} A_{\text{pix}} / \pi)^{1/2}$ , with  $N_{\text{pix}}$  as the number of pixels associated with a given dendrogram leaf and  $A_{\text{pix}}$  being the area of a single pixel. The mass of each catalog source is defined as

$$M_{\text{leaf}} = \frac{d^2 S_{\nu} R_{\text{gd}}}{\kappa_{\nu} B_{\nu}(T_{\text{d}})}, \quad (1)$$

where  $d$  is the distance to the Galactic Center (8.2 kpc, GRAVITY Collaboration et al. 2019),  $S_{\nu}$  is the leaf’s integrated flux,  $R_{\text{gd}}$  is the gas-to-dust ratio (taken to be 100, e.g., Battersby et al. 2011),  $\kappa_{\nu}$  is the dust opacity at frequency  $\nu$ , and  $B_{\nu}(T_{\text{d}})$  is the Planck function evaluated for dust temperature  $T_{\text{d}}$ , as determined from Herschel dust emission modeling (Mills & Battersby 2017). We also derive source-scale column densities from the CMZoom data, calculated for each catalog leaf as

$$N_{\text{H}_2} = \frac{F_{\nu}^{\text{peak}} R_{\text{gd}}}{\mu_{\text{H}_2} m_{\text{H}} \kappa_{\nu} B_{\nu}(T_{\text{d}})}, \quad (2)$$

using the same definitions as above, with  $F_{\nu}^{\text{peak}}$  as the leaf’s peak flux density in Jy beam<sup>-1</sup>,  $\mu_{\text{H}_2}$  as the mean atomic weight (2.8, e.g., Kauffmann et al. 2008), and  $m_{\text{H}}$  as the mass of hydrogen.

Using the total leaf mass  $M_{\text{leaf}}$  defined above in Equation (1), we can estimate the average number density of each leaf by assuming that each leaf’s mass is distributed uniformly with spherical symmetry inside a radius equal to  $R_{\text{eff}}$ . This simplifying assumption yields

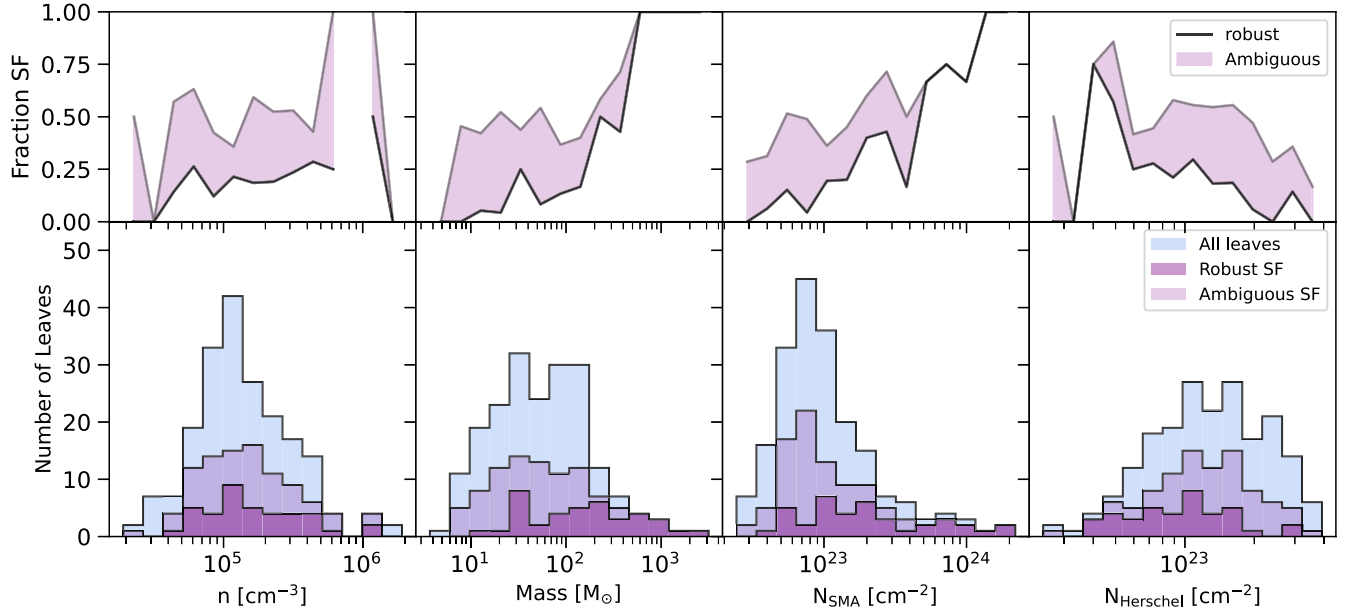
$$n(\text{H}_2) = \frac{3M}{4\pi R_{\text{eq}}^3 \mu_{\text{H}_2} m_{\text{H}}}, \quad (3)$$

from which we can also construct the object’s freefall time,

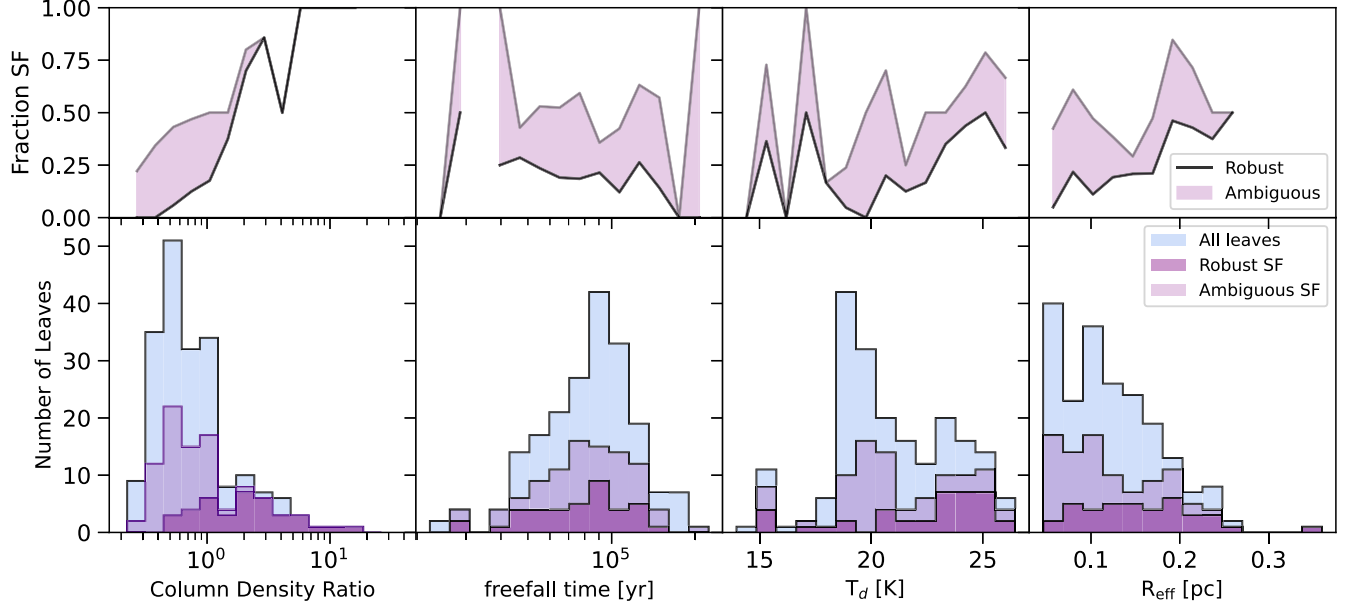
$$t_{\text{ff}} = \left( \frac{3\pi}{32G\mu_{\text{H}_2} m_{\text{H}} n_{\text{H}_2}} \right)^{1/2}, \quad (4)$$

<sup>23</sup> <https://dataverse.harvard.edu/dataverse/cmzoom>

<sup>24</sup> This catalog is on the CMZoom Dataverse at doi:10.7910/DVN/RDE1CH.



**Figure 4.** The physical properties of the robustly star-forming CMZoom catalog objects compared with the properties of all catalog objects (from left to right: volume number density of  $\text{H}_2$ , total leaf mass, peak column density of  $\text{H}_2$  resolved by the SMA, and the cloud-scale column density in  $\text{H}_2$  as measured by Herschel). Each bottom panel shows a binning of the CMZoom catalog’s distribution for the respective property. Each panel shows three histograms: the dark purple histogram shows the distribution of leaves associated with robust tracers of active star formation, the pale purple histogram shows the distribution of leaves with either robust or ambiguous star formation signatures, and the distribution of all leaves is shown in light blue. The solid black line in the upper panels for each physical property shows the ratio between the histogram counts for the distributions of star-forming leaves for each bin, representing the fraction of leaves at that quantity’s value that are robustly forming stars. A region is shown above each of these representing how this fraction increases if we include the ambiguous star formation tracers as well.



**Figure 5.** A continuation of Figure 4. The physical properties of the robustly star-forming CMZoom catalog objects compared with the properties of all catalog objects (from left to right: the column density ratio ( $N_{\text{SMA}}/N_{\text{Herschel}}$ ), the leaf freefall time, the local dust temperature, and the leaf effective radius). Each bottom panel shows a binning of the CMZoom catalog’s distribution in the respective physical properties. Each panel shows three histograms, the dark purple histogram shows the distribution of leaves associated with robust tracers of active star formation, the pale purple histogram shows the distribution of leaves with either robust or ambiguous star formation signatures, and the distribution of all leaves is shown in light blue. The solid black line in the upper panels for each physical property shows the ratio between the histogram counts for the distributions of star-forming leaves for each bin, representing the fraction of leaves at that quantity’s value that are robustly forming stars. A region is shown above each of these representing how this fraction increases if we include the ambiguous star formation tracers as well.

where  $G$  is the gravitational constant and the remaining variables and constants are the same as defined above. The cloud-scale column density used in the following analysis is similarly derived from modeling the SED of dust measured by Herschel, which will be presented in C. Battersby et al. (2024, in preparation). The spatial resolution of this Herschel-derived

column density is  $36''$ , or about 1.4 pc at the distance of the Galactic Center.

In Figures 4 and 5, we consider how the fraction of leaves with indications of active star formation correlates with the catalog properties. For this analysis, we exclude the regions surrounding Sgr B2 and Sgr A. We exclude the former since



**Table 2**  
Summary of the Star-forming Properties for Each Cloud in the CMZ Considering Only Robustly Star-forming Sources

Cloud ID	Colloquial Name	CMZoom Mask Number	SFR <sub>Herschel</sub> $10^{-3} M_{\odot} \text{ yr}^{-1}$	SFR <sub>50 K</sub> $10^{-3} M_{\odot} \text{ yr}^{-1}$	$N_{\text{SF}}$	$N_{\text{SF}}/N_{\text{tot}}$
G1.683-0.089		1	...	...	0	...
G1.670-0.130		2	$3.2 \pm 1.9$	$0.4 \pm 0.2$	2	0.33
G1.651-0.050		3	$1.5 \pm 0.9$	$0.2 \pm 0.1$	1	0.50
G1.602+0.018		4	$4.0 \pm 2.4$	$0.4 \pm 0.3$	1	0.20
G1.085-0.027		5	$6.5 \pm 3.9$	$1.0 \pm 0.6$	2	0.67
G1.038-0.074		6	...	...	0	...
G0.891-0.048		7	...	...	0	...
G0.714-0.100		8	...	...	0	...
G0.699-0.028	Sgr B2	9	...	...	0	...
G0.619+0.012	Sgr B2 SE	10	$30.0 \pm 18.0$	$8.1 \pm 4.9$	7	0.70
G0.489+0.010	Dust Ridge Clouds E&F	11	$15.9 \pm 9.5$	$2.8 \pm 1.7$	1	0.08
G0.412+0.052	Dust Ridge Cloud D	12	...	...	0	...
G0.393-0.034		13	...	...	0	...
G0.380+0.050	Dust Ridge Cloud C	14	$37.9 \pm 22.8$	$10.0 \pm 6.0$	1	0.12
G0.340+0.055	Dust Ridge Cloud B	15	...	...	0	...
G0.326-0.085	The Sailfish	16	...	...	0	...
G0.316-0.201		17	...	...	0	...
G0.253+0.016	The Brick	18	...	...	0	...
G0.212-0.001		19	$5.0 \pm 3.0$	$1.6 \pm 0.9$	3	0.60
G0.145-0.086	The Straw Cloud	20	...	...	0	...
G0.106-0.082	The Sticks Cloud	21	...	...	0	...
G0.070-0.035		22	...	...	0	...
G0.068-0.075	The Stone Cloud	23	$2.2 \pm 1.3$	$0.6 \pm 0.4$	1	0.08
G0.054+0.027		24	...	...	0	...
G0.014+0.021		25	...	...	0	...
G0.001-0.058	The 20 km s <sup>-1</sup> cloud	26	$4.0 \pm 2.4$	$1.2 \pm 0.7$	5	0.26
G359.948-0.052	Sgr A*, circumnuclear disk	27	...	...	0	...
G359.889-0.093	The 50 km s <sup>-1</sup> cloud	28	$32.3 \pm 19.4$	$5.9 \pm 3.5$	1	0.05
G359.865+0.022		29	...	...	0	...
G359.734+0.002		30	...	...	0	...
G359.648-0.133		31	...	...	0	...
G359.611+0.018		32	...	...	0	...
G359.615-0.243		33	...	...	0	...
G359.484-0.132	Sgr C	34	$65.4 \pm 39.2$	$15.4 \pm 9.2$	3	0.60
G359.137+0.031		35	...	...	0	...

**Note.** The first three columns include a coordinate name, colloquial name, and cloud mask index for each cloud. The column “SFR<sub>Herschel</sub>” represents the SFR calculated in Equation (5), assuming a dust temperature from Herschel, as reported in the catalog, with uncertainties due to SFE and random error in the mass estimation. The column “SFR<sub>50 K</sub>” represents the SFR calculated in Equation (5), assuming a dust temperature of 50 K, with uncertainties due to SFE and random error in the mass estimation. The column “ $N_{\text{SF}}$ ” lists the number of robustly star-forming sources within each CMZoom cloud and the final column  $N_{\text{SF}}/N_{\text{tot}}$  lists the fraction of sources with robust star formation tracers in each cloud. For clouds without star formation tracers, and for Sgr B2, these numbers are omitted and replaced with an ellipsis.

(This table is available in machine-readable form.)

the region hosts a particularly massive, more evolved protocluster for which significantly more accurate estimates of SFRs and high-resolution YSO counting and modeling are available (for example, see Schmiedeke et al. 2016 and Ginsburg et al. 2018). We exclude the region surrounding Sagittarius A and the circumnuclear disk due to the highly non-Gaussian noise and contamination from synchrotron emission described in more detail in Battersby et al. (2020). Excluding these regions, we find a total of 39 leaves with a robust signature of active star formation, 57 leaves with ambiguous signs of active star formation, and 104 leaves with a robust non-detection of active star formation. These results are displayed for only robustly star-forming sources in Table 2 and for robustly and ambiguously star-forming sources in Table 3.

#### 4.2. SFRs of CMZ clouds

With a robust estimate of the star formation status of the CMZoom catalog sources, we can derive a new estimate for the SFR of each cloud observed by CMZoom. Hatchfield et al. (2020) calculated an upper limit on the SFR of the CMZ, a star formation potential, in the range of  $0.08\text{--}2.20 M_{\odot} \text{ yr}^{-1}$  (or  $0.04\text{--}0.47 M_{\odot} \text{ yr}^{-1}$  excluding Sgr B2), depending on the assumed SFE. This method makes the assumption that each of the cataloged objects will collapse to form stars on their freefall timescales, which is likely to overestimate the resulting SFRs. By considering which of these sources are associated with active star formation tracers, we can provide a more accurate estimate of the incipient SFR of clouds in the CMZ.

To calculate the incipient SFRs of the CMZoom clouds, we follow a modified version of the procedure used in Hatchfield et al. (2020) for each catalog leaf with a robust star formation

**Table 3**  
A Version of Table 2 Including Ambiguously Star-forming Sources in Addition to Robustly Star-forming Sources

Cloud ID	Colloquial Name	CMZoom Mask Number	SFR <sub>Herschel</sub> $10^{-3} M_{\odot} \text{ yr}^{-1}$	SFR <sub>50 K</sub> $10^{-3} M_{\odot} \text{ yr}^{-1}$	$N_{\text{SF}}$	$N_{\text{SF}}/N_{\text{tot}}$
G1.683-0.089		1	...	...	0	...
G1.670-0.130		2	$3.9 \pm 2.4$	$0.5 \pm 0.3$	4	0.67
G1.651-0.050		3	$1.5 \pm 0.9$	$0.2 \pm 0.1$	1	0.50
G1.602+0.018		4	$5.0 \pm 3.0$	$0.5 \pm 0.3$	3	0.60
G1.085-0.027		5	$7.1 \pm 4.2$	$1.1 \pm 0.6$	3	1.00
G1.038-0.074		6	...	...	0	...
G0.891-0.048		7	...	...	0	...
G0.714-0.100		8	$13.7 \pm 8.2$	$2.7 \pm 1.6$	11	0.44
G0.699-0.028	Sgr B2	9	...	...	0	...
G0.619+0.012	Sgr B2 SE	10	$32.0 \pm 19.2$	$8.6 \pm 5.2$	8	0.80
G0.489+0.010	Dust Ridge Clouds E&F	11	$16.9 \pm 10.1$	$2.9 \pm 1.8$	3	0.23
G0.412+0.052	Dust Ridge Cloud D	12	$2.7 \pm 1.6$	$0.5 \pm 0.3$	2	0.17
G0.393-0.034		13	...	...	0	...
G0.380+0.050	Dust Ridge Cloud C	14	$38.7 \pm 23.2$	$10.2 \pm 6.1$	3	0.38
G0.340+0.055	Dust Ridge Cloud B	15	...	...	0	...
G0.326-0.085	The Sailfish	16	$0.2 \pm 0.1$	$0.1 \pm 0.0$	2	1.00
G0.316-0.201		17	...	...	0	...
G0.253+0.016	The Brick	18	$2.3 \pm 1.4$	$0.4 \pm 0.3$	2	0.18
G0.212-0.001		19	$5.3 \pm 3.2$	$1.6 \pm 1.0$	4	0.80
G0.145-0.086	The Straw Cloud	20	$0.4 \pm 0.3$	$0.1 \pm 0.1$	1	0.50
G0.106-0.082	The Sticks Cloud	21	...	...	0	...
G0.070-0.035		22	$1.7 \pm 1.0$	$0.5 \pm 0.3$	3	0.60
G0.068-0.075	The Stone Cloud	23	$6.4 \pm 3.8$	$1.5 \pm 0.9$	12	1.00
G0.054+0.027		24	...	...	0	...
G0.014+0.021		25	...	...	0	...
G0.001-0.058	The 20 km/s cloud	26	$6.3 \pm 3.8$	$1.8 \pm 1.1$	7	0.37
G359.948-0.052	Sgr A*, circumnuclear disk	27	...	...	0	...
G359.889-0.093	The 50 km/s cloud	28	$50.6 \pm 30.4$	$9.2 \pm 5.5$	9	0.43
G359.865+0.022		29	$0.1 \pm 0.1$	$0.0 \pm 0.0$	1	0.50
G359.734+0.002		30	$0.1 \pm 0.1$	$0.0 \pm 0.0$	1	0.33
G359.648-0.133		31	...	...	0	...
G359.611+0.018		32	...	...	0	...
G359.615-0.243		33	...	...	0	...
G359.484-0.132	Sgr C	34	$65.4 \pm 39.2$	$15.4 \pm 9.2$	3	0.60
G359.137+0.031		35	...	...	0	...

**Note.** The first three columns include a coordinate name, colloquial name, and cloud mask index for each cloud. The column “SFR<sub>Herschel</sub>” represents the SFR calculated in Equation (5), assuming a dust temperature from Herschel, as reported in the catalog, with uncertainties due to SFE and random error in the mass estimation. The column “SFR<sub>50 K</sub>” represents the SFR calculated in Equation (5), assuming a dust temperature of 50 K, with uncertainties due to SFE and random error in the mass estimation. The column “ $N_{\text{SF}}$ ” lists the number of robustly star-forming sources within each CMZoom cloud and the final column  $N_{\text{SF}}/N_{\text{tot}}$  lists the fraction of sources with robust star formation tracers in each cloud. For clouds without star formation tracers, and for Sgr B2, these numbers are omitted and replaced with an ellipsis.

(This table is available in machine-readable form.)

tracer. We translate the properties from the catalog into SFRs for each of the CMZoom clouds as the summation of the individual leaves’ SFRs, using

$$\text{SFR}_{\text{cloud}} = \frac{\epsilon_{\text{SF}}}{\xi_{\text{IMF}}} \sum_i \frac{M_i}{t_{\text{ff},i}}, \quad (5)$$

where the sum runs over the  $i$  leaves in the cloud,  $M_i$  and  $t_{\text{ff},i}$  are, respectively, the mass and freefall time of the  $i$ th star-forming leaf,  $\epsilon_{\text{SF}}$  is the SFE per freefall time, and  $\xi_{\text{IMF}}$  is a correction to account for low-mass star formation to which the CMZoom catalog and the tracers used in this work are not sensitive. In this equation, we make several simplifying assumptions. First, we must choose an average SFE with which these structures are to form stars over the course of a freefall time. We assume that each leaf is forming stars with an

efficiency of

$$\epsilon_{\text{SF}} = 0.25 \pm 0.15 \quad (6)$$

over the course of one of the leaf’s freefall time,  $t_{\text{ff}}$ . The SFE per freefall time has been investigated on the scales of individual protostellar cores ( $\sim 20\%$ – $50\%$ , e.g., Walker et al. 2018; Barnes et al. 2019) as well as on cloud scales ( $\sim 1\%$ – $10\%$ , e.g., Barnes et al. 2017; Leroy et al. 2017; Utomo et al. 2018; Lu et al. 2019b; Krumholz et al. 2019; Chevance et al. 2023; Grudić et al. 2022), but on the intermediate scales investigated in this work, it is unclear what a realistic value might be. The range of values assumed above is intended to be broad enough to encompass a variety of sensible possibilities in agreement with the values estimated for bounding physical scales.

The high-mass star-forming sources characterized here only provide a partially complete picture of the CMZ’s incipient star formation. There is substantial evidence for a lower-mass star-forming population in both the most prolific clouds, such as Sgr B2 (Ginsburg et al. 2018) as well as the supposedly most star formation-deficient clouds, like The Brick (Walker et al. 2021). These lower-mass protostellar populations are not likely to be detectable using the method employed in this work. While the CMZoom catalog is complete to more than 95% of all possible sites of incipient high-mass star formation (the robust catalog is complete to >95% of sources with total gas mass >80  $M_{\odot}$  for an assumed dust temperature >20 K, Hatchfield et al. 2020), it is not sensitive to the population of more isolated low-mass protostars that have been detected in some of the Galactic Center’s molecular clouds.

To account for the missing star-forming mass associated with the lower-mass star protostellar objects in the CMZ, we extrapolate from the stellar IMF (Kroupa 2001) using the IMF python module (<https://github.com/keflavich/imf>). By drawing 1000 samples from the IMF of a cluster with a mass of >100  $M_{\odot}$  (sufficiently above the CMZoom catalogs’ completeness), we find that an average of  $\xi_{\text{IMF}} \approx 20\%$  of the cluster’s star mass is ultimately contained in high-mass protostars.<sup>25</sup> This may be an overestimate for sources that contain significant further fragmentation that includes a significant number of lower-mass protostars, but if the flux detected with the SMA is largely due to dust associated with gas around high-mass protostars, then it is not likely to be a significant overestimate. Future observations capable of measuring the masses of a more complete sample of the CMZ’s protostellar population are necessary to better approximate this value.

The uncertainties for these values are dominated by our assumptions in  $\epsilon_{\text{SF}}$ ,  $\xi_{\text{IMF}}$ , as well as the systematic uncertainties in our assumed value of the gas-to-dust ratio, dust grain properties, and the random uncertainty from noise in the SMA’s flux measurements. The uncertainties in mass, dust temperature, and freefall time are further detailed in Hatchfield et al. (2020). The masses reported in the catalog use dust temperatures calculated from Herschel SED fitting (C. Battersby et al. 2024, in preparation), and therefore apply to a spatial scale of 36”, significantly larger than the size of the CMZoom catalog objects. It is likely that dust temperatures would be systematically higher for sites of active star formation on smaller spatial scales, so the SFRs calculated using the Herschel temperatures may be too high. This is because an assumed lower temperature in Equation (1) implies a higher mass (and similarly a shorter freefall time from Equations (3) and 4), leading to a significantly elevated SFR using Equation (5). Dust temperatures on the scales of individual cores in the CMZ may be higher, 57–220 K or greater (Walker et al. 2018), so we expect the temperatures on the intermediate scales probed by CMZoom to be respectively intermediate to the Herschel-derived values and the core temperatures, though where they fall between these boundary values is difficult to constrain further without higher-resolution observations in the far-IR and submillimeter bands. The values of the SFRs for each cloud are reported in Table 2 assuming both the Herschel-derived temperatures and an intermediate dust temperature of 50 K.

<sup>25</sup> The high-mass stars’ contribution to the total fraction of star mass in a cluster is approximately the same for clusters with mass above 100  $M_{\odot}$ , but may be smaller for low-mass clusters for which the high-mass tail of the IMF is not well sampled.

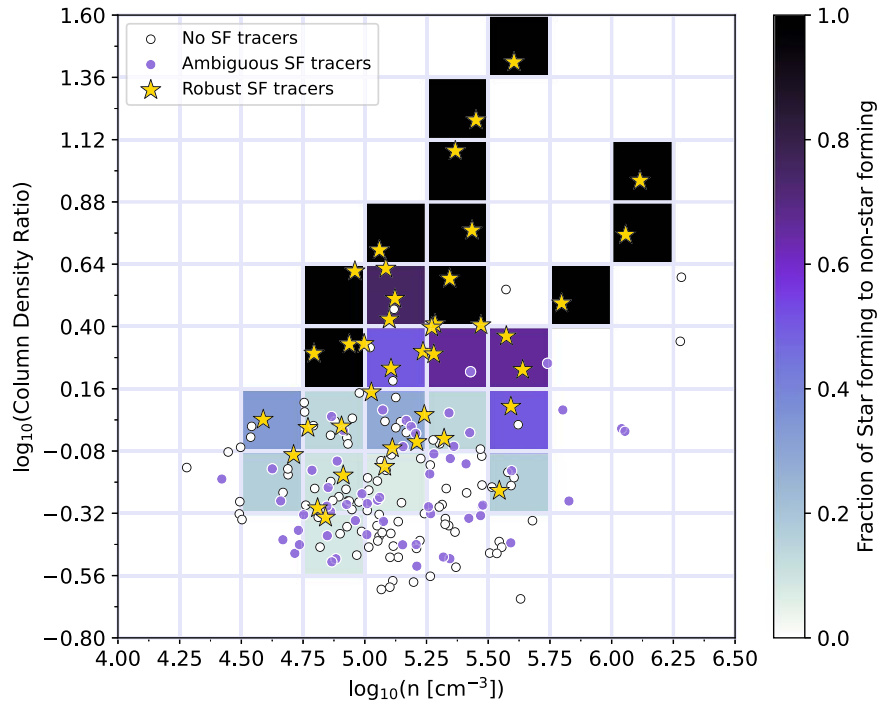
The SFRs of each CMZoom cloud are presented in Figure 7. Due to the considerable uncertainties in the masses of the CMZoom sources within the Sgr B2 complex and the circumnuclear field surrounding Sgr A\*, we exclude these two regions from our analysis (for more details on the issues with the interpretation of these regions see Section 5.1 of Hatchfield et al. 2020 and Section 5.4 of Battersby et al. 2020). While low-mass star formation is likely to occur throughout CMZ clouds both with and without the star formation tracers used in this work, we cannot know their star-forming properties. For the excluded clouds and those with no high-mass star formation indicators, we do not report an SFR, listing “...” instead in Tables 2 and 3.

## 5. Discussion

### 5.1. Number Density, Column Density Ratio, and Their Relationship to Star Formation

Some theories and empirical models of star formation suggest the existence of a volume density threshold (e.g., Krumholz & McKee 2008; Kauffmann et al. 2010; Lada et al. 2010, 2012; Padoan et al. 2014), below which molecular gas cannot efficiently collapse and form new stars. Above this density threshold, some of these theories and models predict an increase in the number of YSOs in the cloud as a scaling relation, their YSO count and therefore SFR increasing with density. The densities of all CMZoom sources appear to be well above the surface and volume density thresholds suggested for solar neighborhood clouds (e.g., Krumholz & McKee 2008; Lada et al. 2010; Clark & Glover 2014). There is also evidence accumulating for the existence of an environmentally dependent density threshold for star formation, which is needed to explain the distribution of star formation observed in CMZ clouds (e.g., Kauffmann et al. 2013; Kruijssen et al. 2014; Rathborne et al. 2014; Kauffmann et al. 2017b; Walker et al. 2018; Lu et al. 2019a, 2019b; Barnes et al. 2019; Battersby et al. 2020). If there exists a universal density threshold above which the amount of star formation increases in proportion to the dense gas mass, we should expect to see a positively correlated scaling relationship, or even a step function relating the density properties of the catalog objects and the prevalence of ongoing star formation. If instead there should be an environmentally dependent threshold, we might expect to see very little star formation below some surface or volume density, and increasingly more star formation above that threshold. Neither of these situations appears to be the case for the CMZoom catalog objects.

In some cases, we do see correlations within the CMZoom sample. Figures 4 and 5 show the fraction of star-forming leaves across the range of physical properties derived in Hatchfield et al. (2020). Three leaf properties do appear to increase significantly along with the prevalence of robust star formation indicators: the total leaf’s mass, the leaf’s peak source-scale column density, and the leaf’s column density ratio (the ratio of the source-scale peak column density to the cloud-scale column density,  $N_{\text{SMA}}/N_{\text{Herschel}}$ ). The uptick in the frequency of star-forming leaves that occurs for both mass and peak source-scale column density is largely due to a very small number of leaves in high-mass and high-column density bins, corresponding to the handful of already well-known and well-studied young massive clusters in the CMZ (Dust Ridge Cloud C, Sgr C).



**Figure 6.** The distribution of robustly star-forming, robustly quiescent, and ambiguous CMZoom catalog leaves as a function of  $n(\text{H}_2)$ , the volume number density of  $\text{H}_2$ , and the column density ratio, defined as the ratio of the SMA-derived source-scale column density to the Herschel-derived cloud-scale column density for each source. The color scale background represents the ratio of star-forming leaves to all leaves in each bin. While leaves with signatures of active star formation occur at both low and high number densities and column density ratios, a sharp uptick in the fraction of star-forming sources occurs at a column density ratio threshold of  $\sim 1.5$  (or  $\log_{10}(\text{column density ratio}) \approx 0.17$ ). There is no obvious scaling between volume density and active star formation.

The sharp rise in the prevalence of robustly star-forming sources that occurs above a column density ratio of  $\sim 1.5$   $N_{\text{SMA}}/N_{\text{Herschel}}$  comes from a significantly larger sample of sources ( $N > 30$ ), including a combination of well-studied regions and previously understudied clouds. Therefore, the column density ratio seems to correlate most significantly with the presence of active star formation. The correlation of column density ratio with the indicators of active star formation is not necessarily surprising (e.g., Kruijssen et al. 2014), as the conditions for active star formation demand the presence of local, gravitationally bound overdensities. Figure 6 shows the stark contrast between the distribution of star formation within leaves as a function of volume density and of column density ratio. While star formation does occur in sources across the range of volume densities and column density ratios probed by CMZoom, the vast majority (over  $\sim 75\%$ ) of leaves above a column density ratio of  $\sim 1.5$  have tracers of star formation. It is possible that this number represents a threshold in the relative surface density, above which turbulent fluctuations are increasingly likely to produce substructures that are dense enough to form stars. While star formation can occur in sources with a low column density ratio, any substructure in excess of this column density ratio threshold is extremely likely to be gravitationally bound and actively forming stars. However, from this study alone it is not possible to determine if this threshold is dependent on the observational parameters of the data used to construct the column density ratio estimate. It is therefore unclear if this can be generalized to a dense gas fraction threshold on similar spatial scales, and further analysis will elucidate its relevance to other surveys of dense substructure in molecular clouds.

Notably, there is no corresponding correlation of star formation tracer prevalence with the volume density of these

sources. The lack of such a correlation with density begs the question—why are stars not preferentially forming in the highest-density substructures? It is possible that the assumptions that we use to derive the leaf volume densities are overly simplistic and fail to accurately represent the importance of the ISM’s three-dimensional complexity. For instance, we assume that the mass derived from each dendrogram leaf’s integrated flux is spherically distributed, and isotropic in both the plane of the sky and along the line of sight. While leaves in the catalog are not uniformly circular, Equation (3) uses the effective radius of each leaf to calculate an average volume density. Densities on the physical scales of the CMZoom are certain to have nonuniformities, and the unresolved substructure of the leaves complicates their interpretation.

Clark & Glover (2014) used hydrodynamic simulations of star-forming clouds to evaluate the efficacy of translating between measured column density and the true volume density of star-forming regions to evaluate star formation density thresholds, finding that the mass of clouds above a given column density does not translate straightforwardly to a mass above a corresponding measured volume density. The average density of a clump-scale object has an inconvenient degeneracy. When averaging over an entire structure composed of unresolved quiescent or star-forming substructure, the mean volume density may represent a log-normal distribution due to the turbulent velocity and density field (as is predicted in the substantial theoretical literature on turbulent molecular clouds, e.g., Chen et al. 2018; Burkhart & Mocz 2019) or it may represent a more diffuse envelope embedding a collection of gravitationally bound cores at very high volume density. Since we cannot distinguish between these scenarios with the mean volume density, one which may either represent a quiescent, turbulent structure, or an actively star-forming object, we

should not expect mean volume density to consistently correlate with star formation tracers. In this way of thinking, the peak SMA column density and the column density ratio are better suited to distinguish between a dense, but unbound structure and an actively star-forming protocluster. This helps to explain why the column density ratio, in the bottom left panel of Figure 5 shows the most robust correlation with active star formation tracers.

It is also possible that the densities measured are an adequate probe of the true volume densities of the sources, and the lack of correlation between volume density and tracers of active star formation is representative of the physical timescales relevant to star formation. The timescales required for protostars to exhibit the star formation tracers used in this work (far-IR radiation from heated gas envelopes and masers) are not well constrained. The flux from which we measure the volume density is not necessarily from material that will form stars, but perhaps also represents gas that is actively escaping the process of star formation. Simultaneously, many of the dense sources that do not exhibit any indication of star formation may truly be pre-stellar gas structures, so the robustly non-star-forming sources may be contributing to future star formation in a way that is not well constrained by this procedure. Higher-resolution observations and virial analysis (e.g., Myers et al. 2022) provide more insight into what component of the gas in these structures should be treated as star-forming or quiescent, though very few sources seem to be entirely gravitationally bound according to the recent spectral analysis presented by Callanan et al. (2023).

### 5.2. Relationship between Tracers of High-mass Star Formation and the Total SFR of the CMZ Clouds

Given the completeness of the CMZoom catalog to sites of incipient high-mass star formation, the SFRs presented in this work effectively incorporate all possible deeply embedded high-mass star formations in the CMZ. If we wish to understand this subset of the star-forming population in the context of the holistic star formation properties of the Galactic Center and calculate an incipient SFR for the CMZ as a whole, we must carefully consider our assumptions about the star formation activity and the protostellar population for which these tracers are not sensitive.

First, the protostellar ages of these star-forming objects are not well constrained. As dense gas in the CMZ's molecular clouds collapses, some local density maxima will achieve the conditions for gravitational instability and collapse to form clusters of stars. The high-mass protostars heat the gas and dust around them and add substantial energy to the surrounding ISM, leading to the emission that we use as a tracer of star formation in this work. Feedback from massive stars in these clusters will begin to erode the cold, submillimeter bright envelope embedding the cluster as photodissociation regions emerge. Therefore, if we see signatures of active high-mass star formation, such as methanol masers or compact dust emission in the far-IR associated with the densest submillimeter bright substructure within a cloud, we know that this star formation has not progressed long enough to destroy or significantly displace its natal envelope. While the amount of time needed for massive YSOs to destroy their envelope is not yet precisely understood and is likely to vary by environment, it is believed that it takes on the order of  $\sim 4 \times 10^5$  yr (Davies et al. 2011).

Therefore, we anticipate that the sources identified in this work probe a range of protostellar ages less than  $\sim 4 \times 10^5$  yr.

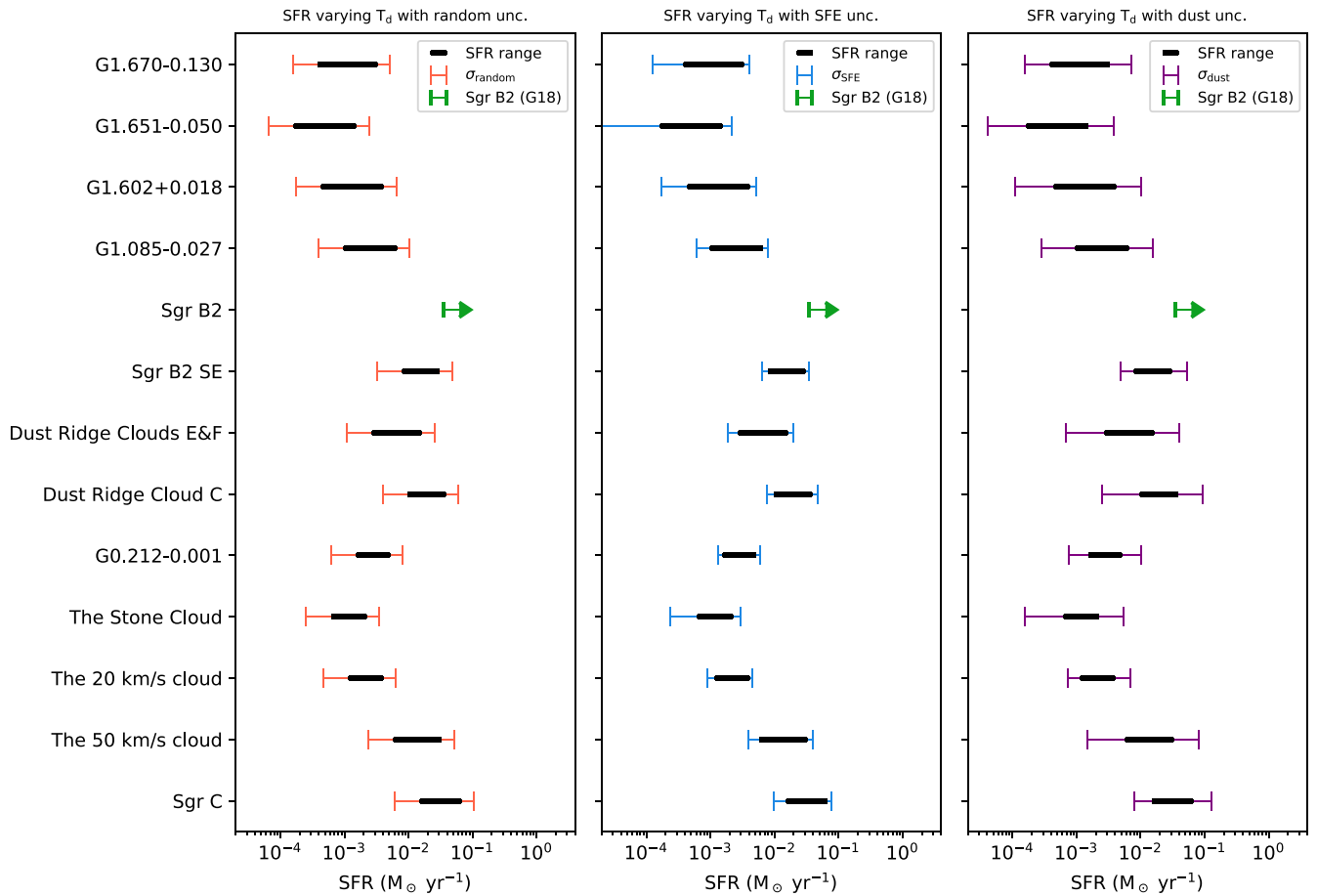
The sample of previously cataloged YSOs used in this work (Yusef-Zadeh et al. 2009; An et al. 2011; Immer et al. 2012) contains many sources that do not correspond to CMZoom catalog sources, likely either representing evolved stellar contaminants or more evolved young high-mass stars that have already destroyed the cold dense components of their envelopes. The presence of a YSO candidate in the absence of compact submillimeter emission, given the completeness of CMZoom, implies that these sources are more advanced in their protostellar evolution. Therefore we expect that CMZoom-associated star formation signatures are tracing a more specific, younger population of protostellar sources, which is how we define the term *incipient* star formation throughout this work.

As discussed briefly in Section 4, the cloud SFRs that we calculate according to Equation (5) rely on ill-constrained assumptions about the SFE per freefall time on these spatial scales and missing lower-mass star formation within the clouds. Given the diverse morphologies and star formation signatures of CMZoom sources, we adopted a range for SFE per freefall time,  $0.1 \leq \epsilon_{\text{SF}} \leq 0.4$  with a fiducial value of 0.25. It is not possible to make a more specific correction due to the IMF than the one used in Equation (5) without a thorough analysis of the low-mass YSO population of the CMZ, which is beyond the capabilities of the present data set but may be feasible with future, higher-resolution and sensitivity observations. There are reports of a top-heavy IMF in the known Galactic Center young star clusters, namely, the Arches, Quintuplet, and Young Nuclear clusters (e.g., Hosek et al. 2019; Rui et al. 2019). While it is still unclear if an abnormal slope is characteristic of nascent CMZ star clusters or high-mass clusters in general, any variation in the typical IMF will influence the assumptions used in calculating these SFRs. A universally top-heavy IMF would imply that the values presented in this work would be overestimates of the true SFRs of CMZ clouds.

With the context of these significant uncertainties, we can estimate the total SFR of the Galactic Center, excluding the circumnuclear disk. Summing over the clouds' SFRs derived in Section 4.2, using our assumed SFE  $\epsilon_{\text{SF}} = 0.25 \pm 0.15$ , the IMF correction described in Section 4.2, and assuming an elevated dust temperature of 50 K, we find an incipient CMZ SFR of  $\sim 0.08 M_{\odot} \text{ yr}^{-1}$  across the 13 robustly star-forming CMZoom clouds. This value includes the SFR for Sgr B2 of  $0.036 M_{\odot} \text{ yr}^{-1}$  calculated by Ginsburg et al. (2018), since the CMZoom observations of the corresponding region are difficult to interpret due to the local noise properties (see Section 5 of Hatchfield et al. 2020 for more details). However, if the dust temperatures on 0.1 pc scales near star-forming sources are closer to the Herschel-calculated dust temperatures, the masses used in Equation (5) are considerably higher. Including the sources with ambiguous star formation tracers (detailed in Section 3.2), and with those lower dust temperatures reported in the catalog, we find a higher total CMZ SFR of  $\sim 0.45 M_{\odot} \text{ yr}^{-1}$  across 20 robustly and ambiguously star-forming CMZoom clouds, which is remarkably similar to the empirical dense gas scaling relation-derived value for the CMZ's SFR ( $\sim 0.46 M_{\odot} \text{ yr}^{-1}$ ) presented in Lu et al. (2019a).

### 5.3. Is Star Formation in the CMZ Episodic?

Previous studies of the CMZ SFR using methods including YSO counting, HII region counting, and integrated light



**Figure 7.** The range of SFRs from robustly star-forming sources and uncertainties derived using a variable dust temperature in calculating source masses, using only robust star formation indicators. In each panel, the black bar represents the SFR from Equation (5) for physical properties calculated using a range of assumed dust temperatures from the Herschel-derived estimate reported in the catalog to a constant 50 K. The error bars in each panel represent the uncertainty due to, from left to right, random uncertainties (including local noise in the measured submillimeter flux, assumed distance, and dust temperature fluctuations), the variation due to our choice of SFE, and lastly the uncertainty in the local dust properties of each source. The lower limit on the SFR from Sgr B2 is shown in green using the constraining values presented in Ginsburg et al. (2018).

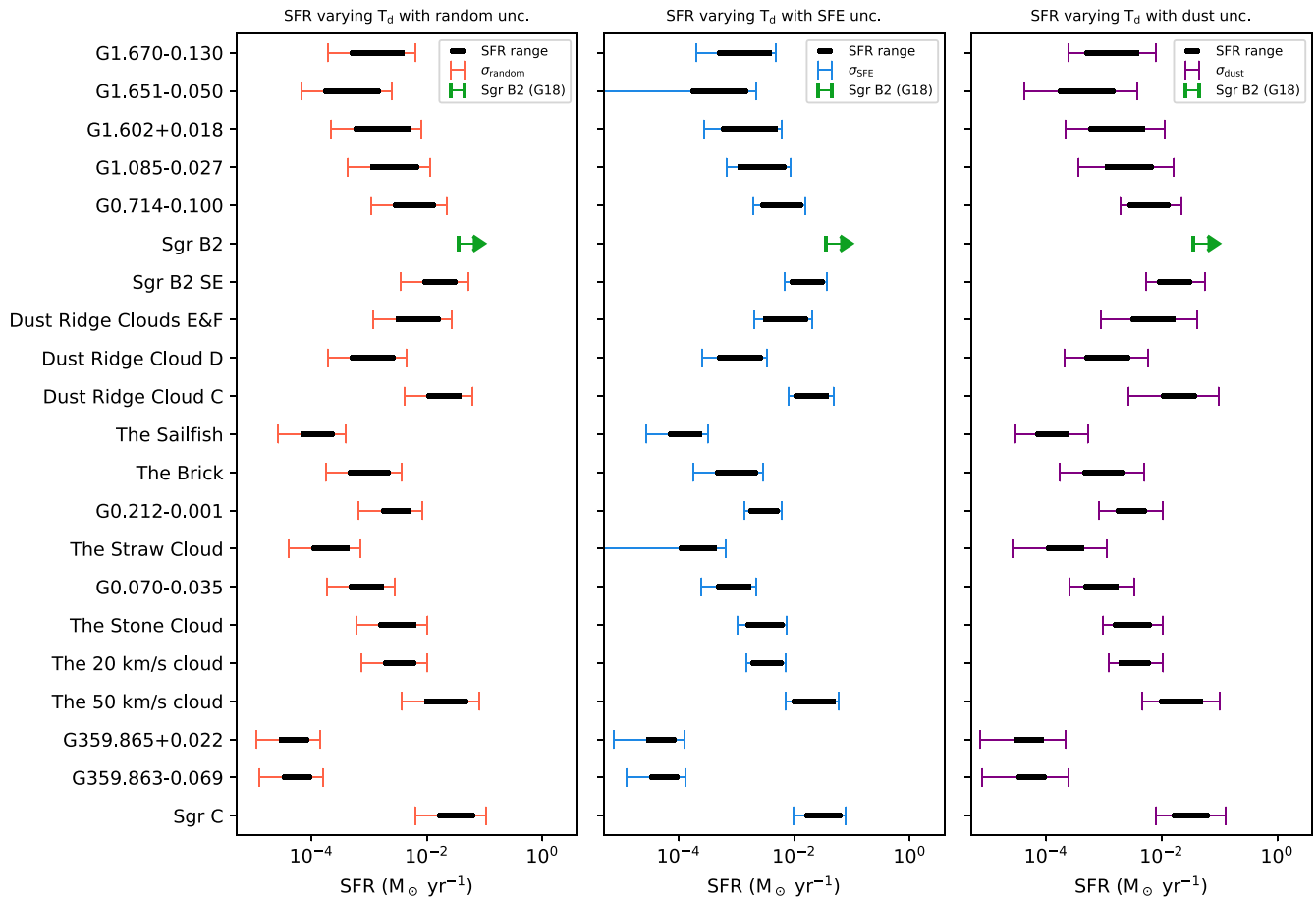
measurements find a CMZ SFR with the mean value computed by Henshaw et al. (2022) of  $0.07_{-0.02}^{+0.08}$ . As stated above, this is in line with our fiducial SFR value of  $\sim 0.08 M_{\odot} \text{ yr}^{-1}$ . However, our fiducial value does not include any ambiguously star-forming sources, and assumes higher dust temperatures than those measured with Herschel, along with an SFE that is very ill-constrained for sources on these spatial scales. If we include the ambiguously star-forming sources, and a higher SFE of 0.4, Equation (5) yields a much higher SFR of  $0.45 M_{\odot} \text{ yr}^{-1}$ , which we can interpret as an upper limit (excluding the uncertainty from the dust temperatures). If these assumed higher values are reasonable and the majority of the ambiguously star-forming sources do host a high-mass protostellar activity, this implies the SFR of the CMZ is increasing.

There is both theoretical and observational precedent for large fluctuations in the Galactic Center’s SFR. Within such a model for the CMZ’s evolution, the dearth of recent star formation is the result of episodic fluctuations, being preceded and followed by periods of enhanced star formation (e.g., Kruijssen et al. 2014; Krumholz & Kruijssen 2015; Armillotta et al. 2019; Orr et al. 2021). As described in more detail in Section 3.2 of Henshaw et al. (2022), there is increasing observational evidence to suggest that the SFR of the CMZ has varied significantly on timescales of tens of megayears (given the stellar masses and ages of the Arches and Quintuplet clusters) and on timescales of

hundreds of megayears. Lu et al. (2019b) suggested that the SFR of the CMZ may show signs of imminently increasing from its present value. In recent work analyzing the stellar age distribution of the nuclear stellar disk, Noguera-Lara et al. (2020) showed that the SFR in the inner few hundred parsecs has reached higher values of  $\sim 0.5 M_{\odot} \text{ yr}^{-1}$  within the last gigayear, similar to the upper limit SFR of  $0.45 M_{\odot} \text{ yr}^{-1}$  calculated in this work.

A recent census of the CMZ’s high-mass star formation using VLA C-band observations of ultracompact H II regions and methanol masers presented in Lu et al. (2019a) finds a lower limit SFR of  $\sim 0.025 M_{\odot} \text{ yr}^{-1}$  for the Galactic Center. The calculation of this value assumes a characteristic timescale of 0.3 Myr and a total stellar mass extrapolated from the IMF. The discrepancy between this and the value presented in our analysis may be due to a difference in the timescale and phase of star formation traced by both methods (the median freefall time for star-forming sources in the CMZ catalog is 0.1 Myr). It is likely that much of the star-forming mass we characterize in this work represents more recent and future star formation, not necessarily associated with observed masers and observable ultracompact H II regions.

Alternatively, we can calculate a much more conservative estimate of the SFR to act as a lower limit on the CMZ’s SFR by neglecting the IMF correction and only considering the mass



**Figure 8.** A version of Figure 7 that also includes ambiguously star-forming sources. Again, in each panel, the black bar represents the SFR from Equation (5) for physical properties calculated using a range of assumed dust temperatures from the Herschel-derived estimate reported in the catalog to a constant 50 K. The error bars in each panel represent the uncertainty due to, from left to right, random uncertainties (including local noise in the measured submillimeter flux, assumed distance, and dust temperature fluctuations), the variation due to our choice of SFE, and lastly the uncertainty in the local dust properties of each source. The lower limit on the SFR from Sgr B2 is shown in green using the constraining values presented in Ginsburg et al. (2018).

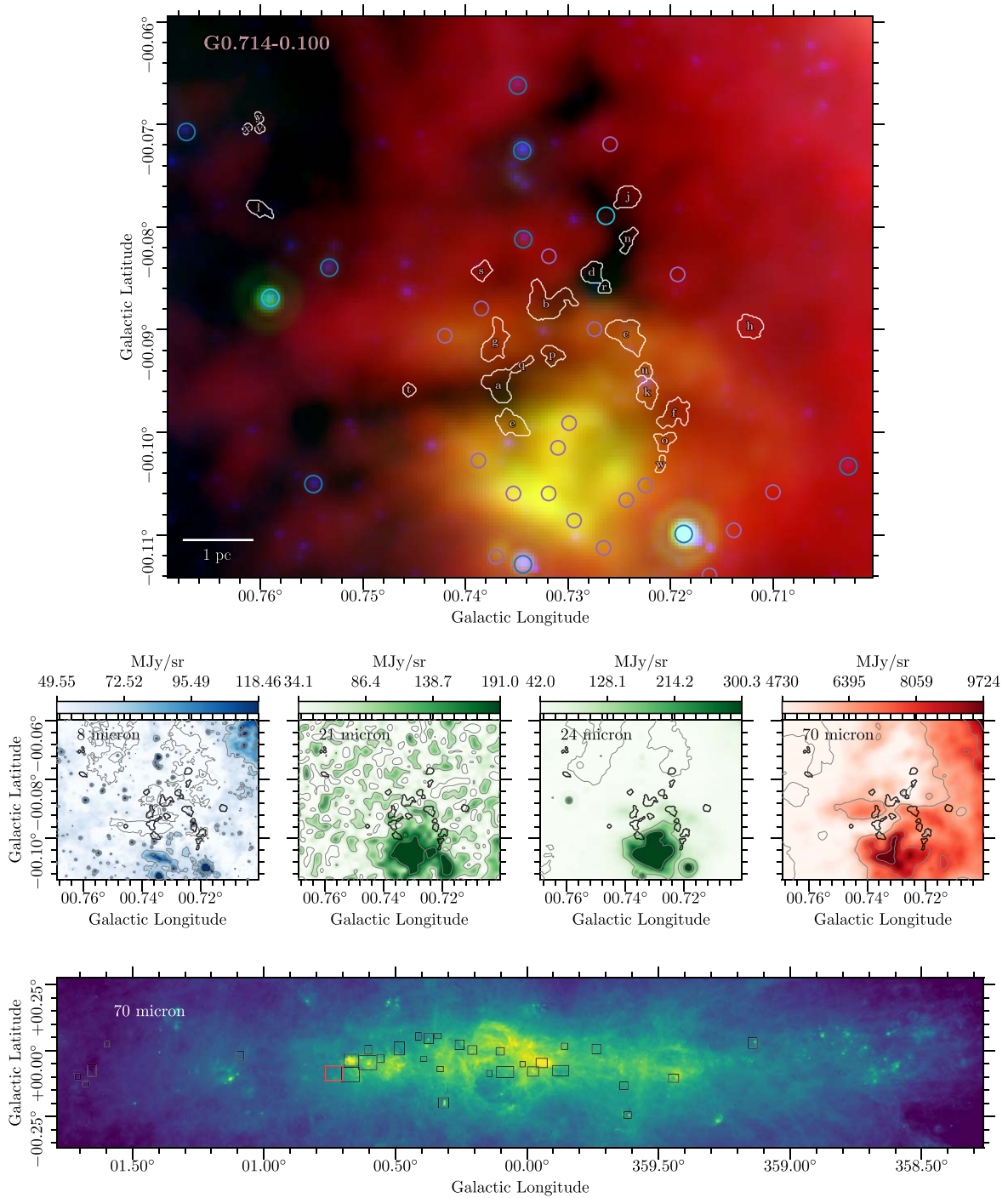
derived from the observed robustly star-forming objects. This lower limit value still depends on the choice of SFE and dust temperature, and as such must still be interpreted with caution. Neglecting the IMF correction, and with an assumed dust temperature of 50 K and a low SFE of 10%, we find a total SFR (excluding the circumnuclear disk (CND)) of  $\sim 0.05 M_{\odot} \text{ yr}^{-1}$ , the majority of which is due to the estimate of the SFR of Sgr B2 ( $\sim 0.036 M_{\odot} \text{ yr}^{-1}$ , from Ginsburg et al. 2018). This lower limit lies much closer to previous estimates of the CMZ’s SFR. The most significant sources of uncertainty in the measurements of cloud SFRs remain the dust opacity, dust temperature, and SFE described in Section 4 and shown in Figures 7 and 8.

#### 5.4. Nature of Atoll Structures in Dense Submillimeter Gas

Amidst the wealth of dense gas morphologies observed throughout the sample of CMZ clouds, several regions exhibit a common pattern of dense submillimeter sources clustered surrounding a more evolved source, reminiscent of an atoll of cold gas islands enclosing a far-IR bright lagoon. These *atoll sources* occur in several clouds surveyed by CMZoom, an example of which is shown in Figure 9. Atoll sources are flagged by eye, as their morphology varies significantly from region to region. It is not obvious that these sources represent a common physical phenomenon or several different phenomena that appear similar on the plane of the sky. Line-of-sight

projection issues rule out any attempt to estimate a completeness to these types of sources, and it is possible that other sources in the catalog would appear as atoll sources from other viewing angles. It is possible that these sources only appear in proximity to their central *lagoon* of compact infrared emission due to plane-of-the-sky projection effects.

In several cases where higher-resolution ALMA data are available, these sources appear to be rings of dense gas surrounding an extended H II region, and therefore represent an interesting phase of molecular cloud evolution. At this point, stellar feedback from young stars is actively eroding their natal envelopes, though it is unclear how long this phase lasts. Parsec-scale bubbles are found in simulations (e.g., Rosen et al. 2021) and observations (e.g., Feddersen et al. 2018) of regions of recent and ongoing star formation, and the lingering presence of a detectable cold dust component to their SEDs may help to constrain their protostellar age and class. Presently, our criteria for identifying these structures are qualitative and a common physical interpretation cannot be argued here, so we aim to simply note their presence and their potential significance. Future work will investigate the properties of these atoll sources and their central H II region lagoons in the combined context of their continuum and spectral properties, taking into account the submillimeter emission along with radio continuum observations using the VLA.



**Figure 9.** An example of the atoll morphology of dust continuum sources observed by CMZoom, shown in the three-color images used for the by-eye classification procedure detailed in Section 3.2. These dust ring configurations are likely to represent the remaining gas surrounding young H II regions. The three colors used in the top panel are 8  $\mu\text{m}$  (blue, GLIMPSE, from Benjamin et al. 2003), 24  $\mu\text{m}$  (green, MIPS GAL, from Carey et al. 2009), and 70  $\mu\text{m}$  (red, Hi-Gal, from Molinari et al. 2010). These are each shown individually in the bottom four panels, along with the 21  $\mu\text{m}$  emission from MSX (Egan et al. 2003). Overlaid on the composite three-color image are white contours outlining the CMZoom leaves, along with cyan circles demarcating YSO candidates from a compilation of those identified by Yusef-Zadeh et al. (2009); An et al. (2011), and Immer et al. (2012), purple circles indicating the 70  $\mu\text{m}$  point sources cataloged by Molinari et al. (2010), and darker blue circles representing the point sources identified by Gutermuth & Heyer (2015). The radial size of these circles corresponds to the FWHM condition used to determine plausible association with CMZoom leaves. The bottom panel shows a 70  $\mu\text{m}$  mosaic of the Galactic Center with each CMZoom region shown as a black box, with the specific region from the above panels highlighted in red.

## 6. Summary

The CMZ hosts a diverse population of giant molecular clouds with different morphologies and fragmented structures, and provides a unique opportunity to study the formation of stars in a more extreme environment than the Galactic Disk.

The CMZoom survey has allowed us to resolve the sub-parsec substructure of all dense material throughout the CMZ. By comparing the highly complete catalog of dense submillimeter sources from this survey with previous wide surveys of signatures of high-mass star formation, we are able to



characterize all possible sites of ongoing, deeply embedded high-mass star formation in the Galactic Center, excluding Sgr B2 and the circumnuclear disk. In this work, we have cross-referenced the CMZoom catalog of submillimeter bright substructure with catalogs of YSO candidates (Yusef-Zadeh et al. 2009; An et al. 2011; Immer et al. 2012) and catalogs of far-IR point sources (Gutermuth & Heyer 2015; Molinari et al. 2016). We also cataloged compact emission localized with the CMZoom catalog leaves in maps of 8 and 24  $\mu\text{m}$  maps from Spitzer, 21  $\mu\text{m}$  maps from MSX, 25 and 37  $\mu\text{m}$  maps from SOFIA’s FORCAST instrument, and 70  $\mu\text{m}$  emission from Herschel by eye. The key results from our analysis are:

1. Of the objects cataloged by CMZoom (excluding the Sgr B2 complex and the CNB region surrounding Sgr A\*), 39 show robust signatures of ongoing high-mass star formation (a maser, previously identified YSO, or by eye identified 24 and/or 70  $\mu\text{m}$  compact sources), while 57 others show ambiguous signatures that may or may not be associated with active star formation. The remaining 103 leaves presently appear robustly quiescent, either representing a very early stage of gravitational collapse without thermal emission in the far-IR, or representing transient, turbulent density fluctuations in the CMZ’s molecular clouds.
2. Assuming a range of star formation efficiencies and local dust temperatures, we calculate a cloud-by-cloud SFR for each region in the CMZoom footprint, sensitive to all sites of recent ( $\lesssim 4 \times 10^5$  yr) and incipient high-mass star formation in the CMZ. Combining these cloud SFRs, we estimate an incipient SFR for the entire CMZ of  $\sim 0.08 M_{\odot} \text{ yr}^{-1}$ . We calculate an upper limit CMZ SFR of  $\sim 0.45 M_{\odot} \text{ yr}^{-1}$ , including more ambiguously star-forming sources, using lower dust temperature estimates and a higher assumed SFE. These SFRs are higher than some previous measurements of the CMZ’s SFR averaged over longer timescales (considerably higher in the lower dust temperature case), suggesting the possibility of an imminent increase in the Galactic Center’s SFR.
3. CMZ sources with higher volume densities are not more likely to host ongoing high-mass star formation. This implies either that denser material is not necessarily more likely to host high-mass star formation, that the densities measured do not accurately represent the densities of the pre-stellar envelope, or that our observational assumptions used to derive a 3D density from the objects’ 1.3 mm dust continuum emission are significantly flawed. Upcoming work constraining gas densities within the CMZoom leaves will help resolve this ambiguity.
4. The gas column density ratio ( $N_{\text{SMA}}(\text{H}_2)/N_{\text{Herschel}}(\text{H}_2)$ ) tends to be higher in regions where high-mass stars are actively forming, particularly above a threshold of  $N_{\text{SMA}}(\text{H}_2)/N_{\text{Herschel}}(\text{H}_2) \gtrsim 1.5$ . It is unclear if this threshold is dependent on the physical scales probed by these particular observations, and thus it should be interpreted with caution.
5. We identify the common morphology of atoll sources, ring-like structures of dense gas surrounding an evolved, far-IR-bright source, resembling a string of islands around a lagoon. Some of these sources correspond to the outskirts of known H II regions. Thus, we suspect these systems represent a particular stage of high-mass

star formation, in which the H II region of a newborn high-mass star is in the process of destroying its natal envelope, and the continuum sources detected are the remaining pockets of dense gas, which may or may not host ongoing or future star formation. These atoll sources may be valuable targets for follow-up studies.

While a great deal of uncertainty remains about the present, past, and future of the CMZ’s SFR, the expansion, and analysis of the CMZoom catalog presented in and published with this work constrains both lower and upper limits on the incipient cloud by cloud and whole CMZ star formation properties. Future observational work will aim to characterize the nature of the ambiguously star-forming sources in the catalog, further constrain dust and gas temperatures on more relevant spatial scales, and better resolve the low-mass component of the CMZ’s YSO population. Simultaneously, further efforts are likely to allow better estimation of a relevant SFE. As our understanding improves, the results from this catalog will continue to constrain the CMZ’s star formation properties, guiding future observations and interpretation of the Galactic Center’s evolution.

### Acknowledgments

We would like to thank the anonymous reviewer for their insightful comments that substantially improved the quality of this work. H.H.’s research was supported by an appointment to the NASA Postdoctoral Program administered by Oak Ridge Associated Universities under contract with NASA. H.H. was supported by JPL, which is run under contract by the California Institute of Technology for NASA. H.H. gratefully acknowledges support for this work from the SOFIA Archival Research Program (program ID 09\_0540). H.H. also thanks the LSSTC Data Science Fellowship Program, which is funded by LSSTC, NSF Cybertraining grant No. 1829740, the Brinson Foundation, and the Moore Foundation; his participation in the program has benefited this work. Additionally, H.H. gratefully acknowledges support from the National Science Foundation under award No. 1816715. E.A.C.M. gratefully acknowledges support from the National Science Foundation under grant No. AST-1813765. A.G. acknowledges support from NSF grants AST 2008101 and CAREER 2142300. C.B. gratefully acknowledges funding from the National Science Foundation under award Nos. 1816715, 2108938, 2206510, and CAREER 2145689, as well as from the National Aeronautics and Space Administration through the Astrophysics Data Analysis Program under Award No. 21-ADAP21-0179 and through the SOFIA archival research program under Award No. 09\_0540. A.T.B. would like to acknowledge funding from the European Research Council (ERC) under the European Union’s Horizon 2020 research and innovation program (grant agreement No. 726384/Empire). J.M.D.K. gratefully acknowledges funding from the European Research Council (ERC) under the European Union’s Horizon 2020 research and innovation program via the ERC Starting Grant MUSTANG (grant agreement No. 714907). COOL Research DAO is a Decentralized Autonomous Organization supporting research in astrophysics aimed at uncovering our cosmic origins. L.C.H. was supported by the National Science Foundation of China (11721303, 11991052, 12011540375, 12233001) and the China Manned Space Project (CMS-CSST-2021-A04, CMS-CSST-2021-A06). Herschel is an ESA space observatory with

science instruments provided by European-led Principal Investigator consortia and with important participation from NASA.

*Software:* This research made significant use of *Astropy* (Astropy Collaboration et al. 2022) This research also utilized *astrodendro*, a Python package to compute dendrograms of Astronomical data (<http://www.dendrograms.org/>) as well as SAO Image DS9 (Joye & Mandel 2003), as well as the python module IMF created by Adam Ginsburg (<https://github.com/keflavich/imf>).

### ORCID iDs

H Perry Hatchfield  <https://orcid.org/0000-0003-0946-4365>  
 Cara Battersby  <https://orcid.org/0000-0002-6073-9320>  
 Ashley T. Barnes  <https://orcid.org/0000-0003-0410-4504>  
 Natalie Butterfield  <https://orcid.org/0000-0002-4013-6469>  
 Adam Ginsburg  <https://orcid.org/0000-0001-6431-9633>  
 Jonathan D. Henshaw  <https://orcid.org/0000-0001-9656-7682>  
 Steven N. Longmore  <https://orcid.org/0000-0001-6353-0170>  
 Xing Lu  <https://orcid.org/0000-0003-2619-9305>  
 Brian Svoboda  <https://orcid.org/0000-0002-8502-6431>  
 Daniel Walker  <https://orcid.org/0000-0001-7330-8856>  
 Elisabeth A. C. Mills  <https://orcid.org/0000-0001-8782-1992>  
 Luis C. Ho  <https://orcid.org/0000-0001-6947-5846>  
 Jens Kauffmann  <https://orcid.org/0000-0002-5094-6393>  
 J. M. Diederik Kruijssen  <https://orcid.org/0000-0002-8804-0212>  
 Jürgen Ott  <https://orcid.org/0000-0001-8224-1956>  
 Thushara Pillai  <https://orcid.org/0000-0003-2133-4862>  
 Qizhou Zhang  <https://orcid.org/0000-0003-2384-6589>

### References

- An, D., Ramírez, S. V., Sellgren, K., et al. 2011, *ApJ*, 736, 133  
 Armillotta, L., Krumholz, M. R., Di Teodoro, E. M., & McClure-Griffiths, N. M. 2019, *MNRAS*, 490, 4401  
 Astropy Collaboration, Price-Whelan, A. M., Lim, P. L., et al. 2022, *ApJ*, 935, 167  
 Barnes, A. T., Longmore, S. N., Battersby, C., et al. 2017, *MNRAS*, 469, 2263  
 Barnes, A. T., Longmore, S. N., Avison, A., et al. 2019, *MNRAS*, 486, 283  
 Battersby, C., Bally, J., Ginsburg, A., et al. 2011, *A&A*, 535, A128  
 Battersby, C., Keto, E., Walker, D., et al. 2020, *ApJS*, 249, 35  
 Benjamin, R., Churchwell, E., Babler, B., et al. 2003, *PASP*, 115, 953  
 Burkhart, B., & Mocz, P. 2019, *ApJ*, 879, 129  
 Callanan, D., Longmore, S. N., Battersby, C., et al. 2023, *MNRAS*, 520, 4760  
 Carey, S. J., Noriega-Crespo, A., Mizuno, D. R., et al. 2009, *PASP*, 121, 76  
 Caswell, J. L., Fuller, G. A., Green, J. A., et al. 2010, *MNRAS*, 404, 1029  
 Chen, H. H.-H., Burkhart, B., Goodman, A., & Collins, D. C. 2018, *ApJ*, 859, 162  
 Chevanne, M., Krumholz, M. R., McLeod, A. F., et al. 2023, in *Protostars and Planets VII, The Life and Times of Giant Molecular Clouds*, ed. S.-i. Inutsuka et al. (San Francisco, CA: ASP), 1  
 Clark, P. C., & Glover, S. C. O. 2014, *MNRAS*, 444, 2396  
 Dahmen, G., Huttemeister, S., Wilson, T. L., & Mauersberger, R. 1998, *A&A*, 331, 959  
 Davies, B., Hoare, M. G., Lumsden, S. L., et al. 2011, *MNRAS*, 416, 972  
 Egan, M. P., Price, S. D., & Kraemer, K. E. 2003, AAS Meeting, 203, 57.08  
 Feddersen, J. R., Arce, H. G., Kong, S., et al. 2018, *ApJ*, 862, 121  
 Ferrière, K., Gillard, W., & Jean, P. 2007, *A&A*, 467, 611  
 Figer, D. F., Najjarro, F., Gilmore, D., et al. 2002, *ApJ*, 581, 258  
 Forster, J. R., & Caswell, J. L. 1999, *A&AS*, 137, 43  
 Ginsburg, A., Henkel, C., Ao, Y., et al. 2016, *A&A*, 586, A50  
 Ginsburg, A., Bally, J., Barnes, A., et al. 2018, *ApJ*, 853, 171  
 GRAVITY Collaboration, Abuter, R., Amorim, A., et al. 2019, *A&A*, 625, L10  
 Grudić, M. Y., Guszejnov, D., Offner, S. S. R., et al. 2022, *MNRAS*, 512, 216  
 Guesten, R., & Downes, D. 1982, *A&A*, 117, 343  
 Gutermuth, R. A., & Heyer, M. 2015, *AJ*, 149, 64  
 Gutermuth, R. A., Myers, P. C., Megeath, S. T., et al. 2008, *ApJ*, 674, 336  
 Hankins, M. J., Lau, R. M., Radoński, J. T., et al. 2020, *ApJ*, 894, 55  
 Hankins, M. J., Lau, R. M., Mills, E. A. C., Morris, M. R., & Herter, T. L. 2019, *ApJ*, 877, 22  
 Hatchfield, H. P., Battersby, C., Keto, E., et al. 2020, *ApJS*, 251, 14  
 Henshaw, J. D., Caselli, P., Fontani, F., et al. 2016, *MNRAS*, 463, 146  
 Henshaw, J. D., Ginsburg, A., Haworth, T. J., et al. 2019, *MNRAS*, 485, 2457  
 Henshaw, J. D., Barnes, A. T., Battersby, C., et al. 2022, in *ASP Conf. Ser. 534, Protostars and Planets VII*, ed. S.-i. Inutsuka (San Francisco, CA: ASP), 83  
 Hinkle, K. H., & Barnes, T. G. 1979, *ApJ*, 227, 923  
 Hosek, M. W., Jr, Lu, J. R., Anderson, J., et al. 2019, *ApJ*, 870, 44  
 Immer, K., Schuller, F., Omont, A., & Menten, K. M. 2012, *A&A*, 537, A121  
 Joye, W. A., & Mandel, E. 2003, in *ASP Conf. Ser. 295, Astronomical Data Analysis Software and Systems XII*, ed. H. E. Payne, R. I. Jedrzejewski, & R. N. Hook (San Francisco, CA: ASP), 489  
 Kauffmann, J., Pillai, T., & Zhang, Q. 2013, *ApJL*, 765, L35  
 Kauffmann, J., Pillai, T., Zhang, Q., et al. 2017a, *A&A*, 603, A89  
 Kauffmann, J., Pillai, T., Zhang, Q., et al. 2017b, *A&A*, 603, A90  
 Kauffmann, J., Bertoldi, F., Bourke, T. L., Evans, N. J., II, & Lee, C. W. 2008, *A&A*, 487, 993  
 Kauffmann, J., Pillai, T., Shetty, R., Myers, P. C., & Goodman, A. A. 2010, *ApJ*, 716, 433  
 Koepferl, C. M., Robitaille, T. P., Morales, E. F. E., & Johnston, K. G. 2015, *ApJ*, 799, 53  
 Krieger, N., Ott, J., Beuther, H., et al. 2017, *ApJ*, 850, 77  
 Kroupa, P. 2001, *MNRAS*, 322, 231  
 Kruijssen, J. M. D., & Longmore, S. N. 2013, *MNRAS*, 435, 2598  
 Kruijssen, J. M. D., Longmore, S. N., Elmegreen, B. G., et al. 2014, *MNRAS*, 440, 3370  
 Krumholz, M. R., & McKee, C. F. 2008, *Natur*, 451, 1082  
 Krumholz, M. R., & Kruijssen, J. M. D. 2015, *MNRAS*, 453, 739  
 Krumholz, M. R., Kruijssen, J. M. D., & Crocker, R. M. 2017, *MNRAS*, 466, 1213  
 Krumholz, M. R., McKee, C. F., & Bland-Hawthorn, J. 2019, *ARA&A*, 57, 227  
 Lada, C. J., Lombardi, M., & Alves, J. F. 2010, *ApJ*, 724, 687  
 Lada, C. J., Forbrich, J., Lombardi, M., & Alves, J. F. 2012, *ApJ*, 745, 190  
 Leroy, A. K., Schinnerer, E., Hughes, A., et al. 2017, *ApJ*, 846, 71  
 Longmore, S. N., Bally, J., Testi, L., et al. 2013a, *MNRAS*, 429, 987  
 Longmore, S. N., Kruijssen, J. M. D., Bally, J., et al. 2013b, *MNRAS Lett.*, 433, L15  
 Lu, X., Zhang, Q., Kauffmann, J., et al. 2015, *ApJL*, 814, L18  
 Lu, X., Mills, E. A. C., Ginsburg, A., et al. 2019a, *ApJS*, 244, 35  
 Lu, X., Zhang, Q., Kauffmann, J., et al. 2019b, *ApJ*, 872, 171  
 Lu, X., Cheng, Y., Ginsburg, A., et al. 2020, *ApJL*, 894, L14  
 Lu, X., Li, S., Ginsburg, A., et al. 2021, *ApJ*, 909, 177  
 Mills, E. A. C., & Battersby, C. 2017, *ApJ*, 835, 76  
 Mills, E. A. C., Ginsburg, A., Immer, K., et al. 2018, *ApJ*, 868, 7  
 Minier, V., Ellingsen, S. P., Norris, R. P., & Booth, R. S. 2003, *A&A*, 403, 1095  
 Miranda, L. F., Gómez, Y., Anglada, G., & Torrelles, J. M. 2001, *Natur*, 414, 284  
 Molinari, S., Swinyard, B., Bally, J., et al. 2010, *PASP*, 122, 314  
 Molinari, S., Schisano, E., Faustini, F., et al. 2011, *A&A*, 530, A133  
 Molinari, S., Schisano, E., Elia, D., et al. 2016, *A&A*, 591, A149  
 Myers, P. C., Hatchfield, H. P., & Battersby, C. 2022, *ApJ*, 929, 34  
 Noguera-Lara, F., Schödel, R., Gallego-Calvente, A. T., et al. 2020, *NatAs*, 4, 377  
 Omont, A., Gilmore, G. F., Alard, C., et al. 2003, *A&A*, 403, 975  
 Orr, M. E., Hatchfield, H. P., Battersby, C., et al. 2021, *ApJL*, 908, L31  
 Padoan, P., Federrath, C., Chabrier, G., et al. 2014, in *Protostars and Planets VI*, ed. H. Beuther et al. (Tucson, AZ: Univ. Arizona Press)  
 Ramírez, S. V., Arendt, R. G., Sellgren, K., et al. 2008, *ApJS*, 175, 147  
 Rathborne, J. M., Longmore, S. N., Jackson, J. M., et al. 2014, *ApJ*, 786, 140  
 Rosen, A. L., Offner, S. S. R., Foley, M. M., & Lopez, L. A. 2021, arXiv:2107.12397  
 Rui, N. Z., Hosek, M. W., Lu, J. R., et al. 2019, *ApJ*, 877, 37  
 Schmiecke, A., Schilke, P., Möller, T., et al. 2016, *A&A*, 588, A143  
 Schuller, F., Ganesh, S., Messineo, M., et al. 2003, *A&A*, 403, 955  
 Schultheis, M., Lançon, A., Omont, A., Schuller, F., & Ojha, D. K. 2003, *A&A*, 405, 51  
 Shetty, R., Beaumont, C. N., Burton, M. G., Kelly, B. C., & Klessen, R. S. 2012, *MNRAS*, 425, 720

- Stetson, P. B. 1987, *PASP*, **99**, 191
- Torrey, P., Hopkins, P. F., Faucher-Giguère, C.-A., et al. 2017, *MNRAS*, **467**, 2301
- Utomo, D., Sun, J., Leroy, A. K., et al. 2018, *ApJL*, **861**, L18
- Walker, D. L., Longmore, S. N., Bastian, N., et al. 2016, *MNRAS*, **457**, 4536
- Walker, D. L., Longmore, S. N., Zhang, Q., et al. 2018, *MNRAS*, **474**, 2373
- Walker, D. L., Longmore, S. N., Bally, J., et al. 2021, *MNRAS*, **503**, 77
- Walsh, A. J., Purcell, C. R., Longmore, S. N., et al. 2014, *MNRAS*, **442**, 2240
- Williams, B. A., Walker, D. L., Longmore, S. N., et al. 2022, *MNRAS*, **514**, 578
- Xu, Y., Li, J. J., Hachisuka, K., et al. 2008, *A&A*, **485**, 729
- Yusef-Zadeh, F., Hewitt, J. W., Arendt, R. G., et al. 2009, *ApJ*, **702**, 178
- Yusef-Zadeh, F., Braatz, J., Wardle, M., & Roberts, D. 2008, *ApJL*, **683**, L147